Bioactive Materials 39 (2024) 544–561

Contents lists available at ScienceDirect

Bioactive Materials

journal homepage: www.keaipublishing.com/en/journals/bioactive-materials

# Targeting nanoplatform synergistic glutathione depletion-enhanced chemodynamic, microwave dynamic, and selective-microwave thermal to treat lung cancer bone metastasis

Man Shu [a,b,g,1], Jingguang Wang [c,1], Ziyang Xu [d,g,1], Teliang Lu [d,g,1], Yue He [d,g], Renshan Li [a,g], Guoqing Zhong [d,g], Yunbo Yan [f], Yu Zhang [d,g,***], Xiao Chu [d,e,g,**], Jin Ke [a,g,*]

[a] Department of Joint and Orthopedics, Orthopedic Center, Zhujiang Hospital, Southern Medical University, Guangzhou, Guangdong, 510282, China
[b] Department of Orthopaedics, General Hospital of Southern Theater Command of PLA, Guangzhou, 510010, China
[c] Department of Biomedical Engineering, School of Materials Science and Engineering, South China University of Technology, Guangzhou, 510640, China
[d] Department of Orthopaedics, Guangdong Provincial People's Hospital, Guangdong Academy of Medical Sciences, Southern Medical University, Guangdong, 510080, China
[e] Medical Research Center, Guangdong Provincial People's Hospital, Guangdong Academy of Medical Sciences, Southern Medical University, Guangzhou, 510080, China
[f] Department of Internal Medicine, Xiang'an Hospital of Xiamen University, School of Medicine, Xiamen University, Xiamen, 361102, China
[g] Guangdong Engineering Technology Research Center of Functional Repair of Bone Defects and Biomaterials, Guangdong, 510080, China

ARTICLE INFO

*Keywords:*
$MgFe_2O_4$@ZOL nanoparticles
Targeting
Chemodynamic therapy
Microwave dynamic therapy
Microwave thermal therapy

ABSTRACT

Once bone metastasis occurs in lung cancer, the efficiency of treatment can be greatly reduced. Current mainstream treatments are focused on inhibiting cancer cell growth and preventing bone destruction. Microwave ablation (MWA) has been used to treat bone tumors. However, MWA may damage the surrounding normal tissues. Therefore, it could be beneficial to develop a nanocarrier combined with microwave to treat bone metastasis. Herein, a microwave-responsive nanoplatform ($MgFe_2O_4$@ZOL) was constructed. $MgFe_2O_4$@ZOL NPs release the cargos of $Fe^{3+}$, $Mg^{2+}$ and zoledronic acid (ZOL) in the acidic tumor microenvironment (TME). $Fe^{3+}$ can deplete intracellular glutathione (GSH) and catalyze $H_2O_2$ to generate •OH, resulting in chemodynamic therapy (CDT). In addition, the microwave can significantly enhance the production of reactive oxygen species (ROS), thereby enabling the effective implementation of microwave dynamic therapy (MDT). Moreover, $Mg^{2+}$ and ZOL promote osteoblast differentiation. In addition, $MgFe_2O_4$@ZOL NPs could target and selectively heat tumor tissue and enhance the effect of microwave thermal therapy (MTT). Both in vitro and in vivo experiments revealed that synergistic targeting, GSH depletion-enhanced CDT, MDT, and selective MTT exhibited significant antitumor efficacy and bone repair. This multimodal combination therapy provides a promising strategy for the treatment of bone metastasis in lung cancer patients.

## 1. Introduction

Lung cancer is the leading cause of cancer-related death worldwide, and approximately 30 %–40 % of lung cancer patients develop bone metastases [1–3]. Due to the invasion of lung cancer cells into the bone matrix, reactive osteogenesis decreases, resulting in osteolytic destruction [4]. As a consequence, nearly half of patients with bone metastases suffer from skeletal-related events (SREs), such as pathological

Peer review under responsibility of KeAi Communications Co., Ltd.
* Corresponding author. Department of Joint and Orthopedics, Orthopedic Center, Zhujiang Hospital, Southern Medical University, Guangzhou, Guangdong, 510282, China.
** Corresponding author. Medical Research Center, Guangdong Provincial People's Hospital, Guangdong Academy of Medical Sciences, Southern Medical University, Guangzhou, 510080, China.
*** Corresponding author. Department of Orthopaedics, Guangdong Provincial People's Hospital, Guangdong Academy of Medical Sciences, Southern Medical University, Guangdong, 510080, China.
*E-mail addresses:* zhangyu@gdph.org.cn (Y. Zhang), chuxiao@gdph.org.cn (X. Chu), kejin332500@163.com (J. Ke).
[1] These authors contributed equally to this work.

https://doi.org/10.1016/j.bioactmat.2024.04.016
Received 6 February 2024; Received in revised form 30 March 2024; Accepted 16 April 2024

fractures, spinal cord compression, severe pain, and hypercalcemia, which can greatly decrease quality of life and increase mortality [5–7]. For patients with lung cancer with bone metastases, the main treatment methods are surgery and chemotherapy, and bisphosphonates (BPs) are often used to treat osteolytic destruction [8]. However, due to the lower blood supply relative to that in other tissues, chemotherapeutic drugs do not easily reach tumor tissue, which affects the efficacy of treatment, and the use of higher doses or continuous use of BPs may induce osteonecrosis of the jaw (ONJ) [9–12]. Therefore, it is imperative to develop a novel therapeutic method for the treatment of bone metastases to reduce the incidence of SREs rates and prevent side effects caused by surgery and chemotherapy.

Hyperthermia can directly damage cancer cells and result in enhanced internalization of chemotherapeutic drugs [13]. Compared to other thermotherapies, microwave ablation (MWA) possesses numerous advantages in tumor treatment, including deep penetration, high heating efficiency, minimal side effects, and effective pain relief associated with cancer [14–16]. MWA induces coagulation necrosis by continuously rotating dipoles under the influence of the electromagnetic field, thereby accomplishing microwave thermal therapy (MTT) [17,18]. However, local hyperthermia may induce thermal damage to the surrounding normal tissues and be limited by the ablation zone [19]. With the development and advancement of nanotechnology, a vast array of microwave-responsive nanomaterials have been developed to boost the efficiency of MTT for tumor treatment [20,21]. For example, Tang et al. prepared microcapsules (mPEG-PLGA) based on the MW sensitizers $MoS_2$ and $Fe_3O_4$ for enhanced MWA to expand the heated area of the tumor [22]. Therefore, employing MW-sensitive agents in the context of MWA for tumor treatment offers a promising therapeutic strategy.

With the in-depth study of magnetic nanoparticles (NPs), they have been widely used in the biomedical field for applications such as targeted drug delivery, magnetic hyperthermia, and cancer diagnosis [23,24]. For example, Feng et al. used a novel Cu–Zr MOF under microwave irradiation to significantly improve the microwave sensitizing effect [25]. Among these NPs, spinel magnesium ferrite ($MgFe_2O_4$) NPs can transport drugs to tumor tissue via the enhanced permeability and retention (EPR) effect and an external magnetic field, and can be used as a MW-susceptible agent for tumor-targeted therapy due to their great biocompatibility and electromagnetic wave heat conversion properties [26–28]. The $MgFe_2O_4$ NPs, serving as promising heterogenous Fenton catalysts, can effectively catalyze $H_2O_2$ into hydroxyl radicals (·OH) [29]. Moreover, due to the weakly acidic and high concentration of hydrogen peroxide ($H_2O_2$) and glutathione (GSH) in the tumor microenvironment (TME) [30,31], chemodynamic therapy (CDT) has attracted much attention because of its tumor selectivity and lack of requirement for complicated therapeutic devices [32,33]. However, CDT faces challenges stemming from the limited catalytic efficiency of the conventional Fenton reaction [34,35]. To enhance CDT efficacy, exogenous stimuli are often integrated [36,37]. Consequently, CDT is commonly paired with hyperthermia methods like photothermal therapy to amplify therapeutic outcomes [38,39]. Among thermal treatments, microwaves offer deeper tissue penetration compared to near-infrared light [40,41]. When combined with $MgFe_2O_4$ NPs, microwaves can expedite the production of cytotoxic reactive oxygen species (ROS) within the tumor microenvironment due to their narrow energy band gap [42]. This therapeutic strategy is termed microwave dynamic therapy (MDT) [43,44]. Hence, it is crucial to develop new approaches that combine $MgFe_2O_4$ NPs with MWA to enhance the MTT effect and achieve effective MDT.

Moreover, in the treatment of bone metastatic tumors, it is crucial to precisely target and eradicate tumors while simultaneously ensuring bone reconstruction [45,46]. BPs, which have a high affinity and selectivity for bone, are often used as adjuvants to treat or prevent SREs [47]. Zoledronic acid (ZOL), classified as a third-generation BP with powerful anti-bone resorption properties, is commonly recommended as the primary treatment option for bone metastasis [48,49]. For example, Qiao et al. synthesized ZOL-encapsulated silica-covered gadolinium-upconversion nanoparticles (NPs) tethered to plumbagin, which could facilitate bone metastasis treatment [50]. Additionally, ZOL not only stimulates the activity of osteoblasts to decrease the incidence of SREs but also promotes tumor cell apoptosis [51]. Hence, delivering a concentrated dose of ZOL directly to the bones could serve as an effective strategy for treating lung cancer-related bone metastases.

This manuscript reports for the first time the use of a combination of a spinel magnesium ferrite nanocarrier and microwave. First, a hollow mesoporous spinel $MgFe_2O_4$ nanoparticle-based drug delivery system with microwave sensitivity and precise antitumor activity was constructed. As shown in Fig. 1A, hollow mesoporous $MgFe_2O_4$ NPs were synthesized via a simple solvothermal method, and the triblock copolymer Pluronic F127 was used as a soft template to shape the mesoporous and spherical nanostructure. Subsequently, ZOL was loaded with the $MgFe_2O_4$ NPs using N,N′-carbonyldiimidazole (CDI) as an activator. As displayed in Fig. 1B, once the $MgFe_2O_4$@ZOL NPs were injected, the $MgFe_2O_4$@ZOL NPs targeted the bone tumor through the influence of their own ZOL and the EPR effect to target bone metastasis. It rapidly decomposed to release the cargos of $Fe^{3+}$, $Mg^{2+}$ and ZOL in the acidic TME and under microwave irradiation. $Fe^{3+}$ could react with intracellular GSH to generate $Fe^{2+}$, which catalyzed $H_2O_2$ to generate •OH, resulting in GSH depletion-enhanced CDT. When used in combination with MW, the process was further accelerated and enhanced, resulting in MDT. Moreover, the released $Mg^{2+}$ and ZOL could stimulate osteogenesis for bone regeneration and inhibit cancer cells. In addition, when exposed to low-power MW irradiation, $MgFe_2O_4$ NPs act as an MW sensitizer to selectively heat tumor tissue, enhancing the effect of MTT while minimizing damage to surrounding tissues. Both in vitro and in vivo experiments demonstrated that synergistic targeting, GSH depletion-enhanced CDT, MDT, and selective-MTT via $MgFe_2O_4$@ZOL combined with MW exhibited excellent efficacy in terms of tumor eradication and osteoblast activation. This approach shows promise as a strategy for treating lung cancer bone metastasis.

## 2. Experimental procedure

### 2.1. Materials

Iron chloride hexahydrate ($FeCl_3·6H_2O$), magnesium chloride hexahydrate ($MgCl_2·6H_2O$), ethylene glycol ($C_2H_6O_2$, >99 %) and methylene blue (MB) were bought from Aladdin (Shanghai, China). Pluronic F-127 was obtained from Sigma-Aldrich (USA). Amine-PEG-Amine, acetonitrile, and sodium acetate (NaAc) were purchased from Sinopharm (Shanghai, China). Zoledronic acid (ZOL), N,N′-carbonyldiimidazole (CDI), and triethylamine were purchased from Macklin (Shanghai, China). N,N-Dimethylformamide (DMF) was purchased from Shanghai Boer Chemical Reagent Co., Ltd. Dulbecco's modified Eagle medium (DMEM), penicillin, streptomycin, fetal bovine serum (FBS), and phosphate-buffered saline (PBS) were obtained from Gibco. FITC-xtra was acquired from ATT Bioquest (USA). Cell Counting Kit-8 and the Annexin V-FITC Apoptosis Detection Kit were purchased from Dojindo (Japan). A Live-Dead Cell Staining Kit (propidium iodide (PI) and calcein-AM) was purchased from Bestbio (China). The total glutathione (GSH) assay kit, alkaline phosphatase (ALP) assay kit, and BCIP/NBT alkaline phosphatase color development kit were all purchased from Beyotime Biotechnology Co., Ltd. (China).

### 2.2. Preparation of $MgFe_2O_4$ NPs

Pluronic F127 (1.0 g) was added to ethylene glycol (40 mL) and agitated at 60 °C until the mixture turned clear. Then, 0.4 g of $MgCl_2·6H_2O$ and 1.08 g of $FeCl_3·6H_2O$ were added. The solution was agitated for 30 min to obtain a uniform solution. Next NaAc (1.2 g) was poured into the uniform mixture and mixed vigorously for 60 min. After sonicating for 10 min, the homogeneous suspension obtained was

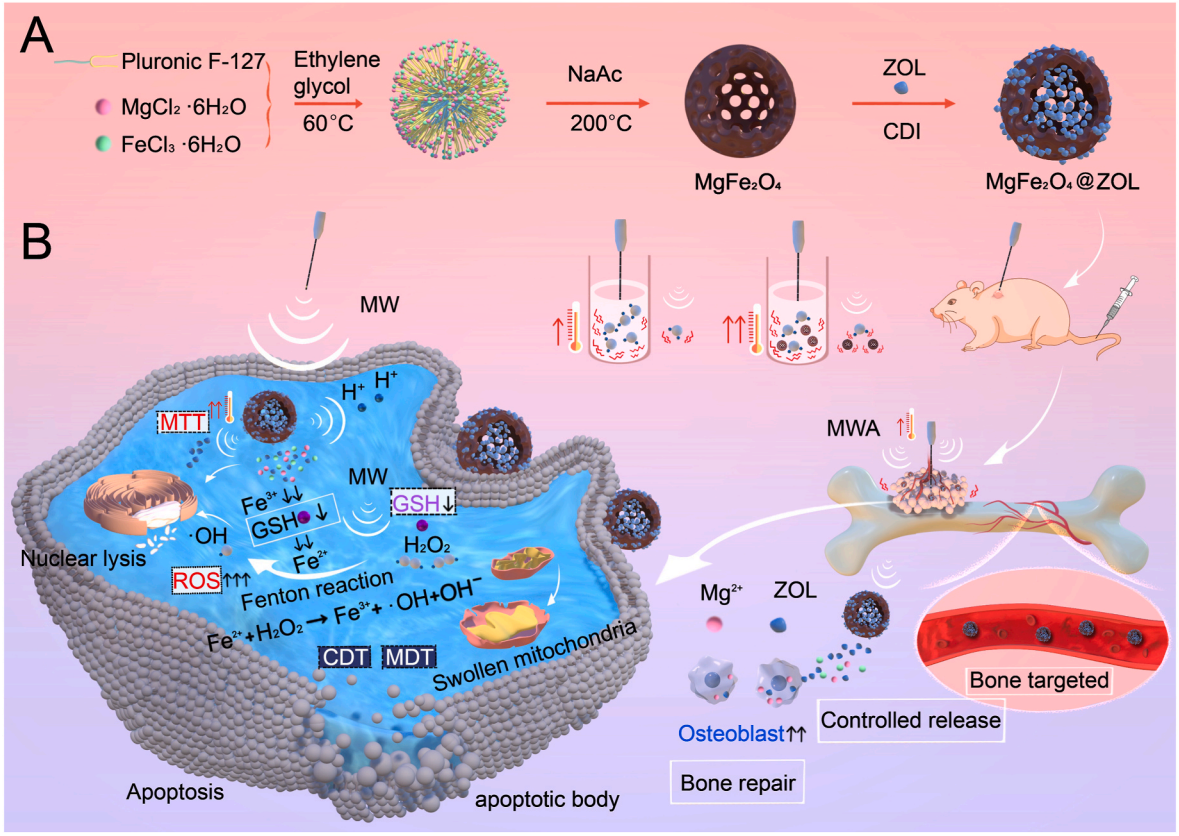


**Fig. 1.** Schematic illustration of the microwave and $MgFe_2O_4$@ZOL NPs used in synergistic tumor therapy. (A) The synthesis process of $MgFe_2O_4$@ZOL NPs. (B) Schematic diagram of synergistic therapy involving targeting, CDT, MDT, and selective-MTT, and bone repair for bone metastasis.

transferred into a 100 mL Teflon-sealed autoclave and put into a vacuum oven at 200 °C for 16 h. The suspension was separated via centrifugation at 10,000 g for 30 min and rinsed three times with distilled water and ethanol to obtain the $MgFe_2O_4$ nanoparticles.

### 2.3. Characterization of $MgFe_2O_4$ NPs

The morphological characteristics of the as-prepared $MgFe_2O_4$ nanoparticles were observed by transmission electron microscopy and scanning electron microscopy (TEM, FEI Talos-F200S, 200 kV; SEM, TESCAN MIRA LMS). X-ray diffraction (XRD) analysis was performed using graphite monochromatized Cu Kα radiation (PANalytical, the Netherlands) at a scanning rate of 5° $min^{-1}$ in the 2θ range of 20–80°. Chemical composition analysis was performed utilizing a Fourier transform infrared (FTIR) spectrometer (iS50, Thermo Fisher Scientific, USA). A Thermo Scientific K-Alpha electron energy spectrometer was utilized to record the X-ray photoelectron spectra (XPS) via Al Kα radiation as the X-ray excitation source. The nanoparticles were dispersed in ethanol and subjected to ultrasonic treatment for 10 min. Subsequently, a Malvern Zetasizer Nano ZS90 system was used to determine the particle size range by dynamic light scattering (DLS) and zeta potential. The Brunauer-Emmett-Teller (BET) surface areas were detected by the typical $N_2$ absorption/desorption method (Micromeritics APSP2460, USA). Thermal analysis of the samples was performed using thermogravimetry (TG; Netzsch, STA 449 C, Germany) under ambient air conditions.

### 2.4. In vitro MW heating effect of $MgFe_2O_4$ NPs

The microwave sensitivity of the $MgFe_2O_4$ NPs was monitored every 30 s using a forward-looking infrared (FLIR) thermal camera. The $MgFe_2O_4$ NPs were dispersed in phosphate buffer saline (PBS) at different concentrations (0, 1, 2.5, 5, and 10 mg/mL) under MW irradiation (5 W, 2450 MHz) for 5 min in vitro. Additionally, changes in the temperature of the $MgFe_2O_4$ NPs solution (1 mg/mL) after microwave irradiation at different powers (0, 3, 4, 5, and 6 W) for 5 min were also observed.

To evaluate the MW thermal stability of $MgFe_2O_4$ NP, a series of MW irradiated cycles were applied. The nanoparticles dispersed in PBS (2.5 mg/mL) was irradiated by MW (5 W) for 5 min. Following this, they were allowed to naturally cool down to room temperature for an additional 10 min for a total of 5 cycles. The temperature change was recorded every 30 s.

### 2.5. ZOL loading and release assays

ZOL was loaded with $MgFe_2O_4$ by modified CDI [52]. First, the amine group was functionalized in $MgFe_2O_4$ NPs by $NH_2$-PEG-$NH_2$. Briefly, $MgFe_2O_4$ and $NH_2$-PEG-$NH_2$ were dispersed at a mass ratio of 2:1 in 10 mL of DMSO, followed by constant shaking for 24 h in the dark. Then, ZOL was activated by CDI. Specifically, 50 mg of ZOL was added to DMF (25 mL) with triethylamine (1 mL). Subsequently, CDI (45 mg) was applied under vacuum for 24 h at 60 °C. The suspension was separated via centrifugation at 10,000 g for 30 min, and the precipitate was collected, which was washed thrice using acetonitrile. Then, $MgFe_2O_4$@ZOL were obtained through an aminolysis reaction between activated ZOL and $MgFe_2O_4$–$NH_2$. In detail, $MgFe_2O_4$–$NH_2$ (25 mg) and activated ZOL (11.3 mg) were dispersed in 10 mL of DMSO in a vessel containing 1 mL of triethylamine under vacuum for 12 h in the dark. Finally, the $MgFe_2O_4$@ZOL NPs were dried in a vacuum oven and collected for subsequent use.

To explore the release behavior of ZOL, the effect of pH on the release rate of ZOL from $MgFe_2O_4$@ZOL was assessed using the dialysis method. Briefly, the $MgFe_2O_4$@ZOL NP solution (200 μL, 2 mg/mL) was sealed in

a dialysis bag with a molecular weight cutoff (MWCO) of 14,000 Da. Subsequently, the bag was placed in a container with 20 mL of PBS (pH = 5.5, 6.5, and 7.4) at room temperature with a shaking rate of 150 rpm $min^{-1}$. At predefined time points, samples of the external PBS solution containing the released ZOL were collected. The amount of ZOL released was calculated by detecting the absorbance at 210 nm via ultraviolet–visible absorption spectroscopy. The standard curves of ZOL were used to calculate the concentration of ZOL. The drug release rate of ZOL from $MgFe_2O_4$@ZOL was determined using the following equation ($M_1/M_2 \times 100$ %), where $M_1$ represents the mass of the released drug in PBS, and $M_2$ represents the weight of the loaded drug.

### 2.6. The bone targeting ability of $MgFe_2O_4$@ZOL NPs

To detect the binding effect of $MgFe_2O_4$@ZOL NPs on bone tissue in vitro, cow bone slices were co-cultured with the same concentration of $MgFe_2O_4$@ZOL NPs and $MgFe_2O_4$ NPs. Cow bone slices were incubated with 100 μg/mL $MgFe_2O_4$ and $MgFe_2O_4$@ZOL NPs, and the contents were stirred slowly. The concentration of $MgFe_2O_4$ NPs was estimated by detecting the absorbance at 563 nm using ultraviolet–visible absorption spectroscopy [53], and then the binding ability was measured by calculating the changes in concentration at various time intervals. The binding rate is equal to the amount of binding to bone divided by the original total.

To further confirm the targeting efficacy of $MgFe_2O_4$@ZOL NPs in vivo, we conducted the live imaging experiment on mouse models with bone metastasis cancer. Initially, we established a lung cancer bone metastasis model in nude mice by administering intraperitoneal injections of 3 % pentobarbital sodium (30 mg/kg) for anesthesia. Subsequently, A549 cells ($10^6$ cells in 20 μL PBS) were directly injected into the left femur using a 26-gauge needle and the nude mice were housed in a specific pathogen-free (SPF) condition. FITC-labeled NPs were then prepared according to the previous literature [54]. 5 μL of FITC-xtra solution (20 mM) was added to 5 mL of $MgFe_2O_4$ and $MgFe_2O_4$@ZOL NPs solutions (1 mg/mL). After stirring on ice for 1 h, the mixture was centrifuged at 10,000 rpm for 5 min to remove unbound FITC-xtra. Subsequently, once the tumor is observed on the left femur of the tumor-bearing mouse compared to the contralateral side, the FITC-labeled NPs were administered to the mouse models via the tail vein (2 mg/kg). Finally, the mice were placed in the IVIS spectrum imaging system (PerkinElmer Instruments Co., Ltd, Shanghai) to capture a series of fluorescence images at different time points (3 h, 6 h, and 24 h).

### 2.7. Detection of singlet oxygen ($^1O_2$) and hydroxyl radicals (·OH) generation

Firstly, the production of singlet oxygen ($^1O_2$) was evaluated by RNO-ID (*p*-nitrosodimethylaniline (RNO)-imidazole (ID)). To elaborate, 0.225 mg RNO and 16.34 mg of ID were added to 30 mL of ultrapure water to form the RNO-ID solution. Then, the RNO-ID solution (500 μL) was added into $MgFe_2O_4$ solution (500 μL) at various concentrations (0, 200, 500, 1,000, and 2000 μg/mL) and the above groups were/were not exposed to MW. The $MgFe_2O_4$ solution (200 μg/mL) was irradiated with MW for different durations. After 4 h of reaction at room temperature, the absorption at 440 nm was detected via a microplate reader.

Methylene blue (MB) can be degraded by ·OH, the production of which can be measured by the change in the absorbance of the MB. Different concentrations of $MgFe_2O_4$ NPs (0, 200, 500, 1,000, and 2000 μg/mL) were added into the MB solution (20 mg/mL) containing 3 % $H_2O_2$, and the absorption values of the mixtures were measured at 664 nm through a UV–vis absorption spectrometer after the reaction occurred for 30 min. Additionally, the production of ·OH was detected at different pH values (pH = 4.5, 5.5, 6.5, and 7.4) and under microwave irradiation (5 W; 0, 1, 2, 3, 4, and 5 min).

In addition, the production of ·OH was detected by the EPR spectrometer, and 5-tert-butoxycarbonyl 5-methyl-1-pyrroline N-oxide (BMPO) was used as the ·OH trapping reagent in this study. The experimental groups were $MgFe_2O_4$, $MgFe_2O_4$ + $H_2O_2$, and MW + $MgFe_2O_4$ + $H_2O_2$. The final concentrations of $MgFe_2O_4$ and $H_2O_2$ were 100 μg/mL and 3 %, respectively. Then, BMPO was added into all the experimental groups, and the mixture was allowed to react for 5 min. The characteristic peaks of ·OH were detected by electron paramagnetic resonance (EPR) spectrometry.

### 2.8. Evaluation of GSH levels and ROS production in cells

A GSH assay kit was used to measure the intracellular GSH level. Human lung adenocarcinoma cells (A549 cells) and solutions containing various concentrations of $MgFe_2O_4$ and $MgFe_2O_4$@ZOL NPs (0, 12.5, 25, 50, 100, and 200 μg/mL) were cocultured. Next, the cells were flushed with PBS and centrifuged at 300 g for 5 min to obtain the sediment. The collected sediment was subjected to two rapid freeze-thaw cycles using liquid nitrogen and ultrapure water at 37 °C to lyse the sediment. The resulting mixture was further centrifuged at 10,000 g for 15 min. Finally, the amount of the supernatant was measured with a GSH assay kit to estimate the intracellular GSH concentration.

The 2′,7′-dichlorodihydrofluorescein diacetate (DCFH-DA) probe was utilized to detect ROS production in cancer cells. A549 cells were incubated in medium supplemented with $MgFe_2O_4$ and $MgFe_2O_4$@ZOL NPs (100 μg/mL). DCFH-DA reagent (10 μM) was added, and the cells were cocultured for 30 min. Subsequently, the cells were rinsed with PBS and irradiated with MW at 5 W for 5 min. The resulting green fluorescence was detected via fluorescence microscopy.

### 2.9. In vitro biocompatibility

The CCK-8 assay was used to assess the cytotoxicity of the $MgFe_2O_4$ NPs. A549 cells, human umbilical vein endothelial cells (HUVECs) and mouse embryo fibroblasts (C3H10) cells, were seeded in 96-well plates ($2 \times 10^3$ cells/well) and treated with various concentrations of $MgFe_2O_4$ NPs (0, 12.5, 25, 50, 100, and 200 μg/mL) for 1, 3, and 5 days. After the respective incubation periods, the cells were flushed twice. Subsequently, a solution consisting of the CCK-8 reagent diluted in DMEM (200 μL, volume ratio = 1:9) was transferred to the well and cocultured for 1 h. The absorption values were measured at 450 nm with a microplate reader to estimate the cell viability.

The biocompatibility of the $MgFe_2O_4$ NPs was assessed by conducting an in vitro hemolysis test. First, fresh rabbit blood containing EDTA was centrifuged at 300 g for 5 min to separate the red blood cells (RBCs). After rinsing with saline, 200 μL of RBCs were diluted to 10 mL with PBS to obtain a 2 % RBC solution. $MgFe_2O_4$ NPs (at various concentrations) (0, 12.5, 25, 50, 100, 200, 400, and 800 μg/mL) were used as the experimental group, PBS was used as a negative control, and ultrapure water was used as a positive control. The contents were mixed gently and incubated at 37 °C for 3 h. Next, the mixtures were centrifuged at 300 g for 5 min, and the optical density (OD) at 545 nm of the supernatant was detected with a microplate reader. The hemolysis rate (%) was determined by the following formula: hemolysis rate (%) = $(OD_M - OD_{NC})/(OD_{PC} - OD_{NC}) \times 100$ %, where $OD_M$ represents the OD of the $MgFe_2O_4$ NPs solution; $OD_{PC}$ represents the absorbance of the positive control; and $OD_{NC}$ represents the absorption of the negative control.

### 2.10. Cytotoxicity and apoptosis analysis of cancer cells under MW irradiation

To evaluate whether $MgFe_2O_4$@ZOL can enhance the efficacy of microwave irradiation of tumors in vitro, cytotoxicity was assessed by the CCK-8 assay and live-dead cell staining. Specifically, A549 cells were cocultured with a range of concentrations (0, 12.5, 25, 50, and 100 μg/mL) of $MgFe_2O_4$ NPs and $MgFe_2O_4$@ZOL NPs for 24 h at 37 °C. Then, the

CCK-8 solution was added to the cells, and the absorbance at 450 nm was detected with a microplate reader. The cell viability was calculated as follows: cell viability (%) = (OD $_{sample}$ - OD $_{blank}$)/(OD $_{control}$ - OD $_{blank}$) × 100.

At the same time, the A549 cells were cocultured with varying concentrations (0, 12.5, 25, 50, and 100 μg/mL) of $MgFe_2O_4$@ZOL NPs for 24 h. After the nanoparticles were endocytosed, the cells were irradiated by microwave at different powers (0, 4, and 5 W) for 5 min. Finally, the A549 cells were continued to culture for 24 h at 37 °C to calculate the cell survival rate using the CCK-8 assay.

In addition, cell viability was observed using a live-dead cell staining kit. A549 cells were cocultured with 100 μg/mL $MgFe_2O_4$ and $MgFe_2O_4$@ZOL NPs for 24 h and then irradiated with MW (5 W, 5 min). Subsequently, the A549 cells were incubated with calcein AM in the dark at 37 °C for 15 min. After two additional flushes, the cells were cocultured with PI for 5 min. Finally, the stained A549 cells were observed by inverted fluorescence microscopy. Subsequently, the number of dead cells and viable cells were counted separately using the ImageJ software.

Flow cytometry was utilized for cell counting to evaluate the apoptosis of cancer cells. First, A549 cells were incubated with $MgFe_2O_4$ and $MgFe_2O_4$@ZOL NPs (100 μg/mL) for 24 h. Furthermore, the cells in the MW group were irradiated with MW (5 W for 5 min) and cultured for an additional 6 h. The adherent cells and the medium were collected and then separated via centrifugation at 300 g for 3 min to obtain all the cells. Subsequently, the collected cells were double rinsed and resuspended in binding buffer. The cell apoptosis rate was analyzed by flow cytometry.

### 2.11. Cellular uptake of $MgFe_2O_4$@ZOL by TEM

The A549 cells were cultured in a cell culture dish for 24 h to allow attachment. After treatment with 100 μg/mL nanoparticles and exposure to MW, the cells were scraped off and rinsed with PBS. The cells were then centrifuged and harvested. Then, 3 % glutaraldehyde and 1 % osmium tetroxide were used to fix the tumor cells for one day. Subsequently, the cells were dehydrated twice using various concentrations of ethanol (50 % and 70 %) and acetone (80 %, 90 %, and 100 %), after which they were incubated for 10 min at each chemical concentration. The dehydrated cells were embedded in Epon812 and polymerized for 48 h at 70 °C. Ultrathin sections of the samples were obtained via an ultramicrotome and treated with lead citrate and uranyl acetate solution. Finally, the sections were observed using TEM.

### 2.12. Colony formation of cancer cells

By evaluating the formation of clones, we assessed the population dependence and proliferation of the cells. First, A549 cells were seeded in a 6-well plate (500 cells per well) and treated with the desired concentration of $MgFe_2O_4$@ZOL NPs and MW as previously described. The cells were then cultured for 14 days, after which the medium was replaced every three days. After the formation of colonies, the proliferating cells were fixed with 4 % paraformaldehyde. Subsequently, crystal violet solution was added to the wells, and the stained cells were rinsed with PBS and photographed.

### 2.13. Cancer cell migration and invasion

The migration ability of cancer cells was assessed via a wound healing assay. After the confluence of the A549 cells reached approximately 90 %, parallel wounds were created on the cell layers via a sterile tool. The cells were incubated with a mixture of nanoparticles and medium for 12 and 24 h, respectively. After incubation, the process of cell migration in the wound area was visualized and documented using a microscope. The migration ratio was determined by calculating the difference in the migration area between the different time points and dividing it by the original area.

Transwell assay was used to assess cell invasion. A549 cells ($1 \times 10^3$ cells) were treated with the abovementioned nanoparticles. The cells were collected and dispersed in serum-free DMEM and then transferred to the upper cavity (pore size: 8 μm). A complete culture solution was poured into the lower plate to support cell growth and to induce cell invasion. After being incubated for 12 h, the cancer cells were fixed using 4 % paraformaldehyde and stained with crystal violet. Images of stained cells were captured through a microscope, and the cells were counted.

### 2.14. Osteoblast differentiation and mineralization assay of C3H10 cells

The potential for osteoblast differentiation was assessed by evaluating the activity of alkaline phosphatase (ALP). First, C3H10 cells were cocultured with a solution containing $MgFe_2O_4$ or $MgFe_2O_4$@ZOL NPs (final concentration: 25 μg/mL). These cells were kept in osteoblast inducer medium (DMEM supplemented with 10 % FBS, 1 % penicillin/streptomycin, 50 μg/mL Vitamin C, 10 mM sodium β-glycerophosphate, and 10 nM dexamethasone, and the prepared induced complete medium was filtered) for 3, 7, and 14 days. Then, the activity of ALP was tested using an ALP color development kit and an ALP assay kit.

Mineralized nodule formation in C3H10 cells was measured by staining the samples with Alizarin Red. After the nanoparticles were endocytosed, the C3H10 cells were cultured in osteoblast inducer medium for 3, 7, or 14 days. Then, the ability to form mineralized nodules was qualitatively analyzed by staining with Alizarin Red and quantitatively evaluated using 10 % hexadecyl pyridinium chloride monohydrate (CPC).

### 2.15. In vivo animal therapeutic efficacy

The Animal Ethics Committee of the General Hospital of Southern Theatre Command authorized all animal experimental procedures (ethical code SYDW2023007). Male BALB/c nude mice (four weeks old) were selected as model animals for tumor studies and housed under specific pathogen-free (SPF) conditions. Lewis lung carcinoma (LLC) cells ($10^6$ cells, 100 μL of DMEM) were administered under the skin near the left scapular region to construct the subcutaneous tumor-bearing mouse model. This injection site was chosen for convenient monitoring and measurement of tumor growth. After the tumor volume reached 50–80 $mm^3$, the mice bearing tumors were randomly allocated into six distinct experimental groups as follows: 1. PBS; 2. $MgFe_2O_4$ NPs; 3. $MgFe_2O_4$@ZOL NPs; 4. PBS + MW; 5. $MgFe_2O_4$ NPs + MW; 6. $MgFe_2O_4$@ZOL NPs + MW. The mice in different groups received tail-vein administration of either PBS (equal to the volume of the solution containing NPs) or a solution containing nanoparticles (2 mg/kg body weight). After 24 h, the mice in the MW groups received microwave ablation at 5 W for 5 min. The temperature variation induced by the MW was monitored using the FLIR instrument. The weight and tumor dimensions of the experimental animals were recorded every three days. The size of the tumors was determined using the following formula: tumor volume = 0.5 × length × width × width. After 14 days, the mice were humanely euthanized. The organs (i.e., the heart, liver, lungs, spleen, and kidneys) and tumors were collected. The tumor tissues were embedded in paraffin and sliced for different staining procedures, including HE, TUNEL, Ki67, and Prussian blue staining. The major organs of the experimental animals were also sectioned for H&E staining. Finally, all stained slices were observed under a fluorescence microscope.

### 2.16. Statistical analysis

All results were derived from repeated independent experiments and are expressed as the mean ± standard deviation (SD). The differences among groups were determined by analysis of variance (ANOVA). All

differences were considered to be statistically significant at $p < 0.05$; * indicates $p < 0.05$, ** indicates $p < 0.01$, *** indicates $p < 0.001$, and **** indicates $p < 0.0001$.

## 3. Results and discussion

### 3.1. Synthesis and characterization of $MgFe_2O_4$ and $MgFe_2O_4$@ZOL

$MgFe_2O_4$ NPs were constructed using a straightforward solvothermal method. The XRD pattern (Fig. 2A) of the sample aligned with the spinel ferrite crystal structure (JCPDS card No.01-071-1232), confirming its chemical formula as $MgFe_2O_4$. The inverse spinel structure of $MgFe_2O_4$ was determined by the distinctive peaks observed in the crystallographic planes (220), (311), (400), (511), and (440) [55]. The characteristic type-IV isotherms with H1 hysteresis loops validate the hollow and mesoporous structure of the $MgFe_2O_4$ (Fig. 2B). The BET-specific surface area of the hollow $MgFe_2O_4$ was determined to be 63.78 $m^2\ g^{-1}$, and the adsorption average pore diameter was about 5.17 nm, as determined by the pore dimension range plot (Fig. 2B and C). From the SEM and TEM images, the as-obtained $MgFe_2O_4$ NPs showed a uniform morphology. They were spherical and had a rough surface; the average size of the particles was about 300 nm, indicating their good dispersibility and homogeneity (Fig. 2D and E). Furthermore, TEM images indicate that the prepared $MgFe_2O_4$ NPs exhibit an inner hollow structure alongside surface mesopores. The presence of a larger surface area and mesoporous structure in $MgFe_2O_4$ NP enabled it to possess a significantly enhanced loading capacity. The selected area electron diffraction (SAED) pattern, spinel structure, and single-crystal nature of the magnesium ferrite particles are shown in Figure S1A-C [55]. The SAED patterns showed that the crystal structure agreed with the structure obtained via XRD. The EDS elemental mapping (Figure S1D) analysis showed that the Fe, Mg, and O elements were uniformly distributed in the as-synthesized $MgFe_2O_4$ nanoparticles. Results from the EDS spectra demonstrated that Mg, Fe, and O was present (Figure S2 and Table S1). Based on the XPS analysis, besides Fe, Mg was also detected in the as-synthesized $MgFe_2O_4$ (Fig. 2H). From the deconvolution, it could be concluded that magnesium existed as $Mg^{2+}$ and iron existed as $Fe^{3+}$ in the $MgFe_2O_4$ nanoparticles. The average particle size of $MgFe_2O_4$ measured by DLS was around 330 nm (Fig. 2K). The zeta potential of the nanoparticles was −30.8 mV (Fig. 2L). To summarize, the hollow mesoporous $MgFe_2O_4$ NPs that could be used for drug loading were synthesized.

As $MgFe_2O_4$ NPs had a special hollow mesoporous structure, they were suitable for drug delivery [56]. In our study, ZOL was efficiently loaded into the hollow and mesopores of $MgFe_2O_4$ NPs through physical adsorption. Moreover, a covalent linkage (amide bond) was also established to conjugate ZOL, resulting in the formation of $MgFe_2O_4$@ZOL NPs. Visual inspection of SEM and TEM images confirmed the presence of a distinct ZOL membrane on the surface of $MgFe_2O_4$@ZOL NPs (Fig. 2D and E). Moreover, TEM analysis revealed that the internal hollow and surface mesoporous structures of $MgFe_2O_4$@ZOL NPs were not readily discernible, indicating successful filling of ZOL within the hollow pores and surface mesopores of $MgFe_2O_4$ NPs. Elemental mapping of $MgFe_2O_4$@ZOL NPs exhibited characteristic P and N elements associated with ZOL (Fig. 2F). The presence of specific peaks corresponding to ZOL in the FTIR spectra of $MgFe_2O_4$@ZOL at 1000-1200 $cm^{-1}$ and 3100-3200 $cm^{-1}$ further validated the effective loading of ZOL (Fig. 2G). Additionally, a comparative analysis of high-resolution XPS spectra of N1s pre- and post-conjugating of ZOL demonstrated a new deconvoluted peak at 399.3 eV, indicating the formation of amide bonds between ZOL and $MgFe_2O_4$ (Fig. 2I). Thermal analysis revealed a drug mass fraction of 32.21 % on $MgFe_2O_4$@ZOL NPs, which exhibited larger size and higher electronegativity compared to $MgFe_2O_4$ NPs (Fig. 2J-L). Collectively, these findings provide strong evidence supporting the successful loading of ZOL onto $MgFe_2O_4$ NPs by absorption physically and the formation of amide bonds.

### 3.2. Microwave heating efficiency in vitro

Magnetic spinel nanoparticles as polar materials can enhance the efficiency of MW heating, and enhance heat through hysteresis losses activated in magnetic fields released from MWA (Fig. 3A) [57,58]. The spinel $MgFe_2O_4$ NP, which is soft magnetic mental oxide, can absorb microwave due to its narrow energy band gap, great magnetic heating capability, and lower thermal conductivity, resulting in low heat loss during heating [59]. Therefore, $MgFe_2O_4$ NPs are suitable heating agents. The property of microwave thermal conversion was evaluated using an FLIR imaging instrument. When the concentration of $MgFe_2O_4$ NPs was 1, 2.5, 5, and 10 mg/mL, as indicated by the infrared images recorded by FLIR (Fig. 3B), the temperature changed to 36.1, 37, 39, and 40 °C, respectively, whereas the temperature of the control group was only 33 °C (Fig. 3C). The above data demonstrated that the temperature of the solution increased in proportion to the concentration of $MgFe_2O_4$. The temperature exhibited a positive correlation with the microwave power when the same concentration of 1 mg/mL $MgFe_2O_4$ NPs was irradiated for 5 min (Fig. 3D) (the infrared thermal images are shown in Fig. 3E). In addition, the microwave thermal stability of $MgFe_2O_4$ NPs (2.5 mg/mL) was analyzed by five irradiation cycles at the power of 5 W. As shown in Fig. 3F, no attenuation in the heating efficiency was demonstrated, illustrating that $MgFe_2O_4$ NPs possess potential for cyclic MWA in antitumor process. These results shown the excellent microwave heating effect of $MgFe_2O_4$ NPs in the simulated body fluid and laid the determining the concentration and microwave power in subsequent experiments. It has been reported that temperatures ranging from 43 to 48 °C can induce apoptosis and necrosis in tumor cells [60]. The 5 W and 6 W groups met the temperature requirement for damaging tumor cells, and the power of the 6 W group was not acceptable due to easy damage to the surrounding tissue. $MgFe_2O_4$ NPs reportedly possess photothermal and magnetic hyperthermia capabilities [59,61], but there have been no reports on the combination of $MgFe_2O_4$ NPs and MW. Due to the greater penetration of MWs compared to that of near-infrared light, MWs can be applied to deep tissue tumors [62]. Both photothermal heating and alternating magnetic fields (AMF) rely on stimulating the inherent heat generation of $MgFe_2O_4$, resulting in limited heating efficiency. However, when $MgFe_2O_4$ NPs are combined with MW, both water and $MgFe_2O_4$ generate heat, significantly enhancing the local temperature elevation effect. $MgFe_2O_4$ exhibits superparamagnetism and a narrow hysteresis loop, making it a promising candidate biomaterial for hyperthermia therapy in cancer [63].

### 3.3. Drug release in vitro

The loaded capacity and pH-triggered release of $MgFe_2O_4$ NPs were assessed via the concentration of ZOL. The drug release concentration was determined using the standard concentration curve of ZOL (Figure S41). The successful loading of ZOL was confirmed by detecting an absorption peak at approximately 210 nm following the coupling of $MgFe_2O_4$ NPs and ZOL (Fig. 3G). The amount of ZOL released from the $MgFe_2O_4$@ZOL NPs increased as the pH decreased (Fig. 3H). The drug was released in short bursts within the initial 10 h, followed by a sustained slow release of the drug. The release rate and quantity of ZOL were greatly greater at pH 5.5 than at pH 7.4, which indicated that the hydrogen ion ($H^+$) concentration of the mixture and the release kinetics of ZOL from the $MgFe_2O_4$@ZOL NPs were positively correlated. On the one hand, due to the large specific surface area of hollow mesoporous structure of $MgFe_2O_4$ NP, which allows for the absorption of ZOL onto material. On the other hand, in the acidic environment, protons protonate the amide bonds in $MgFe_2O_4$@ZOL NP and collapse the mesoporous framework, thereby accelerating drug release [37,64].

### 3.4. The bone targeting ability of $MgFe_2O_4$@ZOL NPs

A major hindrance to cancer therapy is nonspecific action, which can

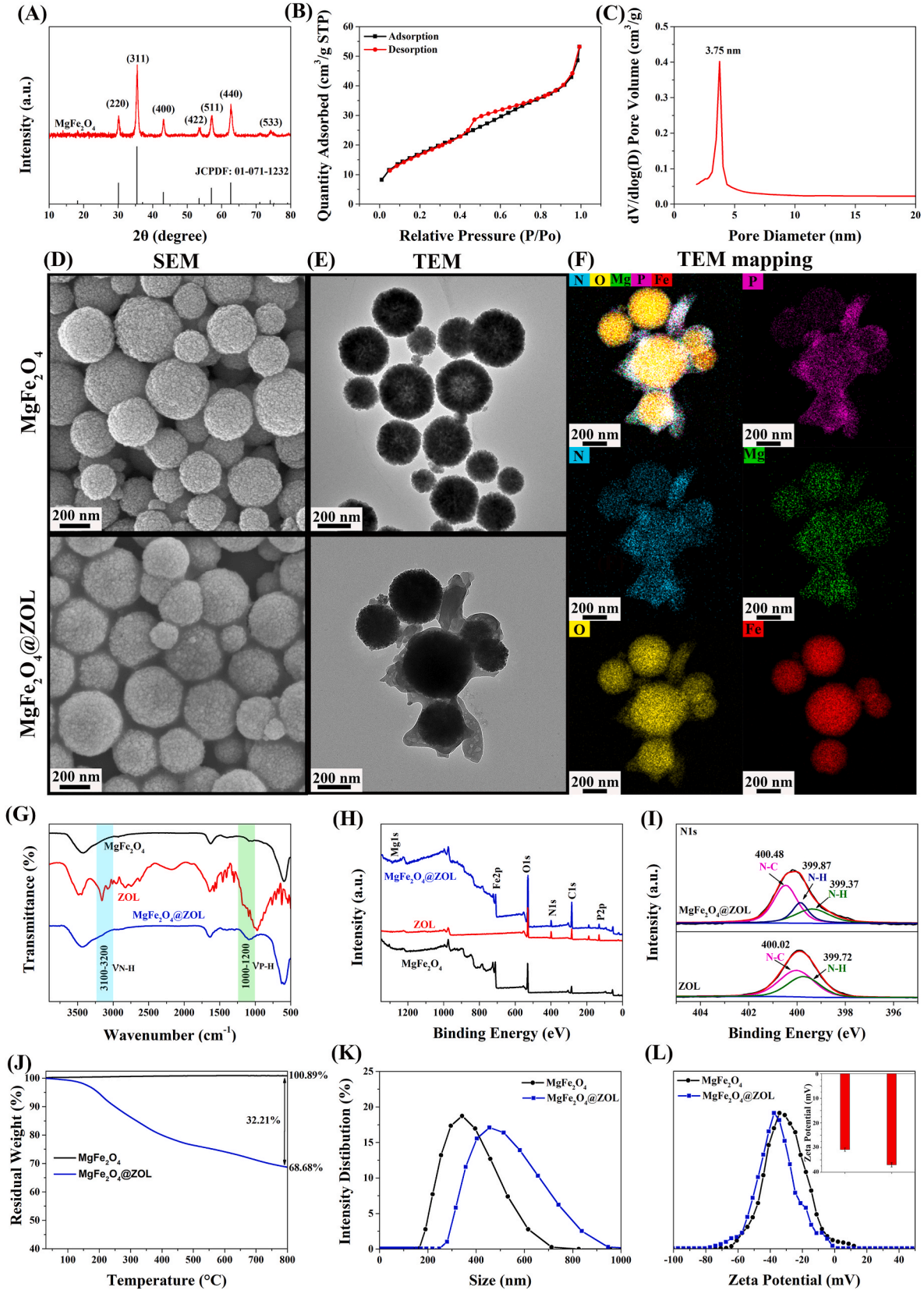


**Fig. 2.** Synthesis and characterization of $MgFe_2O_4$ and $MgFe_2O_4$@ZOL NPs. (A) XRD pattern; (B) $N_2$ absorption/desorption isotherms; (C) pore size distribution curves; (D) SEM image; (E) TEM image; (F) TEM element mapping; (G) FTIR spectra; (H) XPS survey; (I) high-resolution XPS spectra of N1s; (J) TG analysis curves; (K) DLS; (L) Zeta potential.

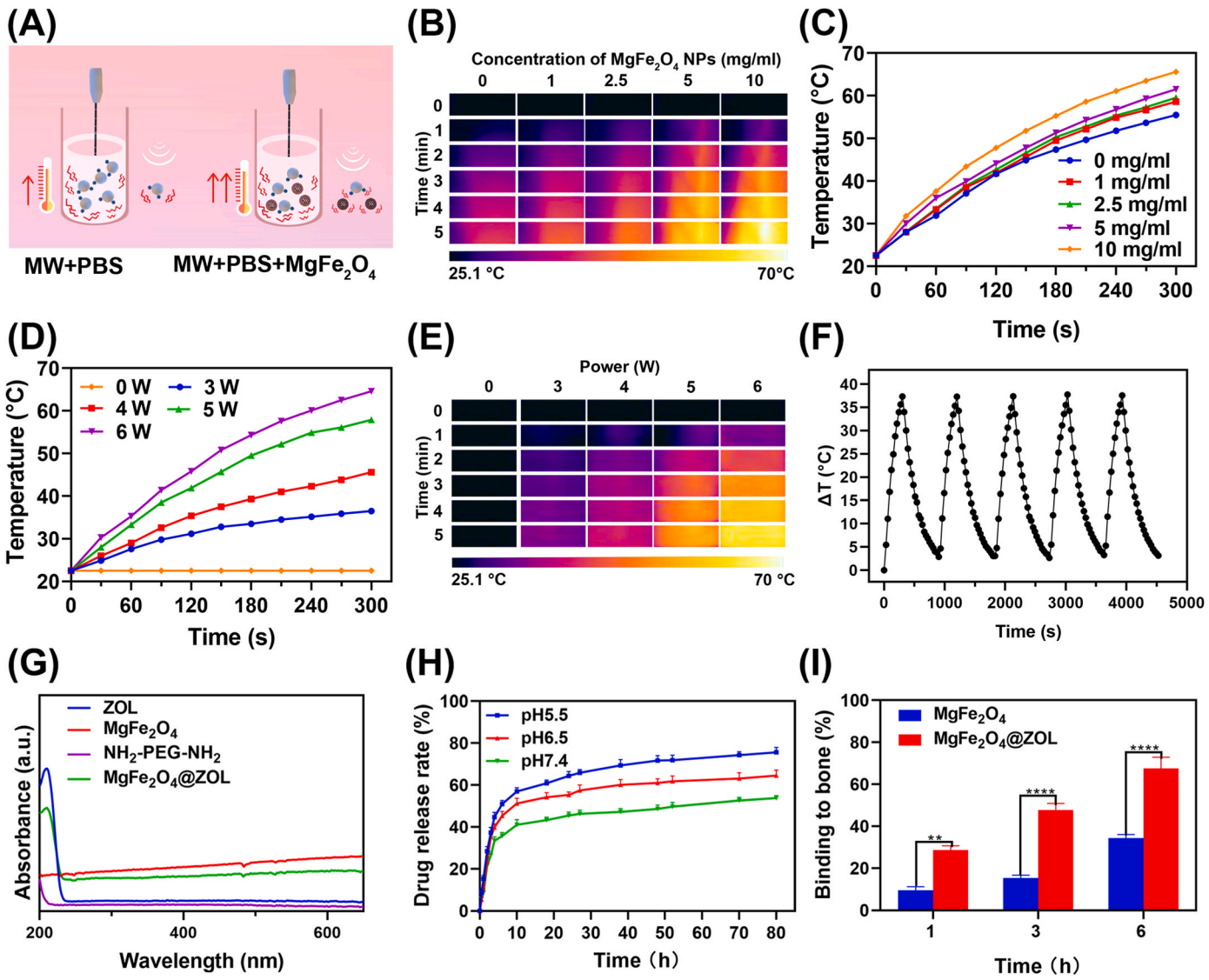


**Fig. 3.** In vitro microwave heating effect of $MgFe_2O_4$ and release of $MgFe_2O_4$@ZOL. (A) The principle of microwave heating. (B) FLIR images of concentration gradients of $MgFe_2O_4$ NPs when the suspension was exposed to MW irradiation. (C) Temperature variations of $MgFe_2O_4$ NPs suspension at different concentrations when the solution was exposed to MW at 5 W for 5 min. (D) Changes in the temperature of the $MgFe_2O_4$ NPs suspension (1 mg/mL) at different microwave power. (E) Infrared thermal images of $MgFe_2O_4$ NPs irradiated by microwave at different power levels. (F) Microwave thermal stability of $MgFe_2O_4$ NPs (2.5 mg/mL) under MW irradiation (5 W) for 5 on-off cycles. (G) The UV–vis spectra of ZOL, $MgFe_2O_4$, $NH_2$-PEG-$NH_2$, and $MgFe_2O_4$@ZOL. (H) The release curves of $MgFe_2O_4$@ZOL NPs at various acid environments. (I) The in vitro bone affinity of $MgFe_2O_4$ and $MgFe_2O_4$@ZOL NPs.

lead to serious problems in patients [52]. As shown in Fig. 3I, $MgFe_2O_4$@ZOL NPs had a stronger affinity for cow bone slices than $MgFe_2O_4$ NPs in vitro. After 6 h, 67.6 % of the $MgFe_2O_4$@ZOL NPs were found in bone slices, while 34.3 % of the $MgFe_2O_4$ NPs were localized in bone slices.

We further assessed the targeting capability of $MgFe_2O_4$@ZOL towards bone tumors in vivo using the aforementioned tumor-bearing mice. These mice were divided into the $MgFe_2O_4$-FITC group and the $MgFe_2O_4$@ZOL-FITC group. Nanoparticles were administered via the tail vein, and fluorescence images were captured using an animal live imaging system after 3, 6, and 24 h, respectively. As illustrated in Figure S3A, the fluorescence intensity was stronger in the 3 h groups compared to the 6 and 24 h groups. Moreover, at the same time points, the fluorescence signals at the bone tumor sites (left femur) were notably more concentrated and intense in the $MgFe_2O_4$@ZOL group. In vivo imaging conducted 6 h after injection of the $MgFe_2O_4$ NP group revealed the presence of fluorescence in certain areas of the tumor site. This could be attributed to the EPR effect of $MgFe_2O_4$ nanoparticles, allowing some nanoparticles to accumulate at the tumor site, while the EPR effect is relatively limited due to the larger particle size of $MgFe_2O_4$ NPs [5,27]. Additionally, $MgFe_2O_4$@ZOL not only exploits the EPR effect but also benefits from the strong bone tumor targeting ability of ZOL, resulting in more concentrated fluorescence signals at the bone tumor sites [65]. Mice in the 3 h post-injection group were euthanized, and vital organs (heart, liver, spleen, lungs, kidneys) and lower limbs were collected for fluorescence imaging. Consistent with the live imaging results, the $MgFe_2O_4$@ZOL group exhibited the most concentrated fluorescence signals at the tumor site (Figure S3B). It was also noted that the nanoparticles were primarily concentrated in the gallbladder and liver, followed by the kidneys. This suggests that the liver and kidneys are the main organs for nanoparticle metabolism and excretion. The aforementioned findings demonstrate that $MgFe_2O_4$@ZOL NPs possess the ability to effectively target bone tumors.

### 3.5. Catalytic production of ROS and consumption of GSH

The $MgFe_2O_4$ NPs reacted with $O_2$ to produce $^1O_2$ under microwave irradiation. The intermediate product of the reaction between $^1O_2$ and imidazole oxidizes RNO, resulting in the solution fading, which is the RNO decolorization reaction [36]. As shown in Figure S4B, at the same concentration, the $MgFe_2O_4$@ZOL group produced more $^1O_2$. The OD of RNO decreased as the concentration of $MgFe_2O_4$ increased and as the MW increased (Fig. 4A). As the duration of exposure to MW increased, a corresponding decrease in the absorption values was recorded after treatment with 200 μg/mL $MgFe_2O_4$ (Figure S4C). It was found that both $MgFe_2O_4$, ZOL, and MW can stimulate ROS production as previously reported [66,67].

GSH, a major endogenous antioxidant that can weaken the Fenton/Fenon-like reaction by depleting the generated ·OH, plays a key role in the tumor antioxidant defense system [68,69]. Therefore, improving the scavenging ability of intracellular GSH in cancer cells can augment the effectiveness of CDT [70]. Due to the killing effect of MW, the MW group was not used in this experiment. The consumption of intracellular GSH was evaluated using a GSH assay kit. The depletion of GSH in tumor cells increased with increasing concentrations of $MgFe_2O_4$ NPs (Fig. 4B), whereas treatment with $MgFe_2O_4$@ZOL resulted in a greater decrease in intracellular GSH. These findings indicated that $MgFe_2O_4$ can enhance the effect of CDT by depleting intracellular GSH. Other studies also reported that ZOL can induce perturbations in the biosynthesis of GSH [67,71,72]. The GSH content in cancerous cells is essential for tumor development and drug resistance [73]. $MgFe_2O_4$@ZOL NPs can deplete GSH by redox reactions to produce $Fe^{2+}$ and GSSH, both of which are toxic to cancer cells, achieving the efficient antitumor effect of GSH depletion-enhanced CDT.

$MgFe_2O_4$ NPs can be used for real-time detection of high concentrations of MB dye as nanocomposites [74]. However, in this study, MB degradation experiments were performed to assess the catalytic efficiency of $MgFe_2O_4$ NPs on the production of ·OH. In the present study, $H_2O_2$ was added to the MB solution to mimic the tumor microenvironment. With increasing concentrations of $MgFe_2O_4$ NPs and $H^+$, the absorption of MB decreased significantly (Fig. 4C and D). Additionally, the blue color faded as the duration of MW irradiation increased (Figure S4D). These results confirmed that $MgFe_2O_4$ NPs can catalyze the production of ·OH from $H_2O_2$. The efficiency of $MgFe_2O_4$ NPs on the

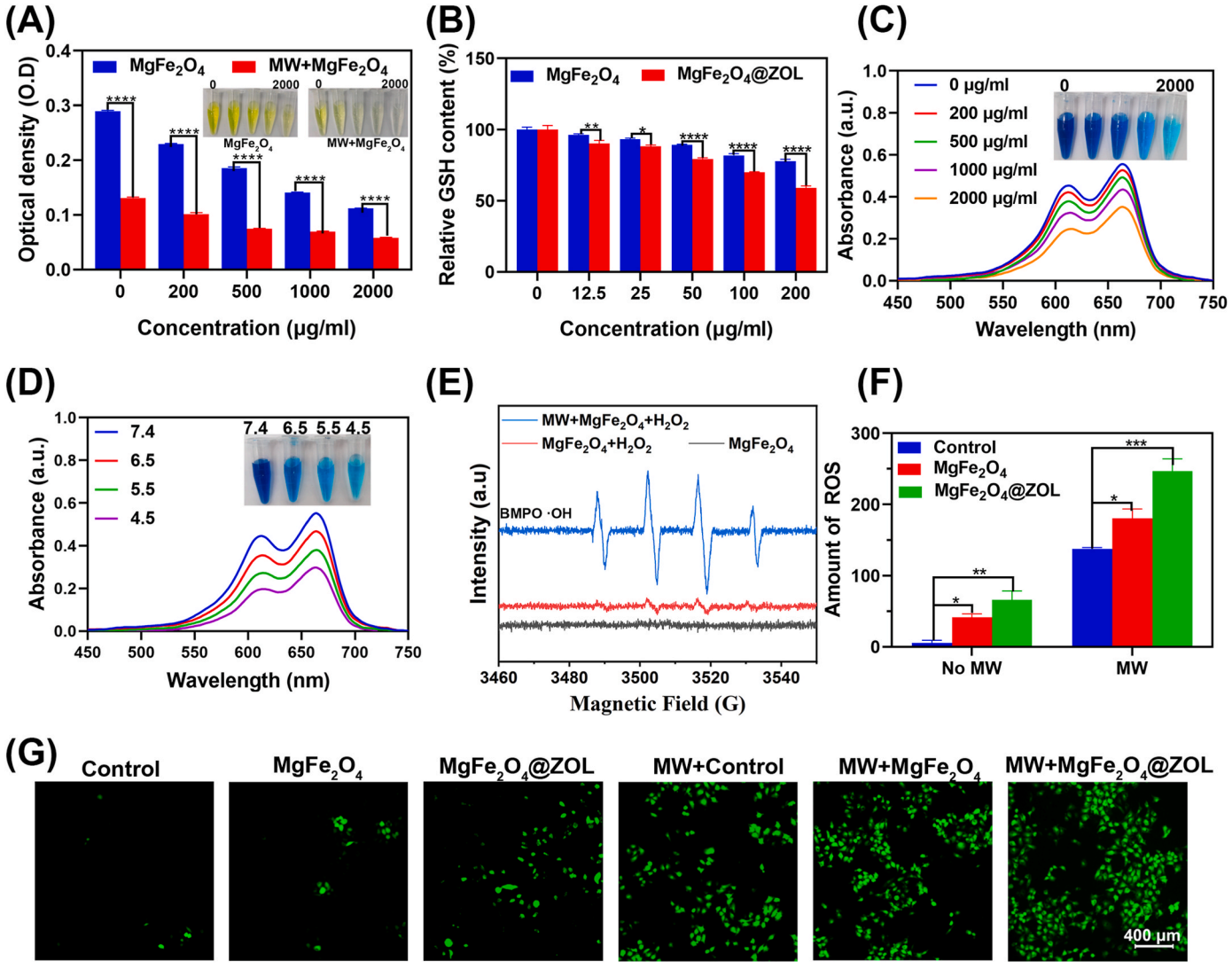


**Fig. 4.** Oxidation-reduction reactions of nanomaterials. (A) Generation of singlet oxygen after treatment with different concentrations of $MgFe_2O_4$ NPs (0, 200, 500, 1000, 2000 μg/mL) and irradiation of MW. (B) The relative GSH content in cancer cells after treatment with various concentrations of $MgFe_2O_4$ or $MgFe_2O_4$@ZOL NPs (0, 12.5, 25, 50, 100, and 200 μg/mL). (C and D) UV–vis absorbance of MB treated with a gradient of concentrations of $MgFe_2O_4$ NPs or acidic environment (insert: images of MB solutions; the concentrations separately are 0, 200, 500, 1000, and 2000 μg/mL; PH are 4.5, 5.5, 6.5, and 7.4). (E) EPR detection of $MgFe_2O_4$ under MW irradiation to produce ·OH. (F) The quantity of cellular ROS produced after different treatments. (G) Fluorescence images illustrating ROS in cells.

production of ·OH increased under acidic conditions and MW irradiation.

The ·OH signal was trapped by BMPO and measured by EPR spectroscopy. The characteristic peaks of ·OH were not detected in the solution containing $MgFe_2O_4$ NPs (Fig. 4E). However, these peaks were detected when $H_2O_2$ was added, which suggested that $MgFe_2O_4$ can catalyze the formation of ·OH by the iron-based Fenton reaction. The intensity of the characteristic peaks of ·OH increased significantly after MW irradiation increased, which indicated that MW irradiation accelerated the Fenton reaction to produce ·OH, thus facilitating MDT. Many studies have reported that MW can accelerate the Fenton reaction [66]. The surface area and temperature of the NPs increased under MW irradiation, and the Fenton reaction rate was also enhanced, thus increasing the efficiency of the $MgFe_2O_4$ NPs for the formation of ·OH [75].

The ability of $MgFe_2O_4$@ZOL combined with MW to catalyze ROS production through intracellular Fenton reactions was investigated using the probe DCFH-DA. The A549 cells treated with the nanoparticles exhibited more intense green fluorescence than did the control cells (Fig. 4F and G), which indicated that $MgFe_2O_4$@ZOL NPs damage cancer cells through CDT [72], and that the overproduction of ROS is generated by ZOL [67,71,72]. The cells irradiated with MW exhibited more intense green fluorescence than those that were not irradiated with MW. These results indicated that ROS production increased considerably after microwave irradiation, and the cells treated with $MgFe_2O_4$@ZOL and exposed to MW irradiation experienced considerably greater ROS production due to the effects of MDT [66,75]. These findings showed that $MgFe_2O_4$@ZOL NPs under MW irradiation have an excellent ability to stimulate ROS production.

Traditional treatments for bone metastasis include chemotherapy, radiation, surgery, and medication. However, the limited number of drugs that can successfully reach bone tumor sites often leads to severe side effects. Therefore, a novel cancer treatment strategy known as CDT utilizes the specific properties of the TME to induce the Fenton reaction in vivo, effectively generating ·OH, which induces tumor cell death [76]. Compared to traditional therapy, CDT demonstrates excellent tumor selectivity and regulates the hypoxic and immunosuppressive TME [77]. $MgFe_2O_4$ NPs, as heterogeneous Fenton catalysts, could increase the rate at which $H_2O_2$ transforms into ROS (such as ·OH and $^1O_2$) [78]. In this paper, the release of $Fe^{3+}$ by $MgFe_2O_4$, while depleting GSH, can induce the Fenton reaction in lung cancer tissues, generating ROS to induce the apoptosis of tumor cells, thereby effectively reducing the side effects of treatment [79]. MTT increases the sensitivity of tumor cells to heat, resulting in thermal damage to tumor tissues. Additionally, the increase in temperature in the tumor area can promote the Fenton reaction, resulting in enhanced CDT [39]. In addition, microwave energy can induce local resonance coupling to create hot spots in specific areas. These hot spots may cause structural changes within the substance, such as the formation of point defects or weak surface bonds, resulting in the generation of free radicals [62]. Thus, we deduced that $MgFe_2O_4$@ZOL NPs create hot spots under MW irradiation and local thermal stimulation to dissociate or modify molecules, ultimately accelerating ROS expression via a similar process. As the above experimental results indicate, this combination therapy can synergize effectively with GSH depletion-enhanced CDT/MDT to generate a large amount of ROS, effectively achieving satisfactory tumor therapeutic effects.

### 3.6. Biocompatibility and toxicity of $MgFe_2O_4$@ZOL NPs and MW in vitro

To use $MgFe_2O_4$ NPs as carriers to deliver ZOL for precision therapy, they should have low toxicity, but they may induce toxicity after exposure to MW irradiation. Therefore, first, the biocompatibility of the $MgFe_2O_4$ NPs was assessed through hemolysis tests and CCK-8 assays. The biocompatibility of the $MgFe_2O_4$ NPs (at different concentrations) (0, 12.5, 25, 50, 100, and 200 μg/mL) for 1, 3, and 5 days, was evaluated after they were co-cultured with A549 cells (Fig. 5A), HUVECs (Figure S4E), and C3H10 cells (Figure S4F). The minimum cell viability was approximately 85 % after the cells were cocultured with 100 μg/mL $MgFe_2O_4$ NPs for five days, which showed that the $MgFe_2O_4$ NPs were highly biocompatible. Hemolysis tests were also conducted on solutions of $MgFe_2O_4$ NPs (12.5, 25, 50, 100, 200, 400, and 800 μg/mL) using rabbit blood. The blank and standard controls consisted of PBS and deionized water, respectively. At all tested concentrations of $MgFe_2O_4$ NPs, the hemolysis rates were less than 1 % (Figure S4G), which indicated the strong biocompatibility and negligible effect of these NPs on the erythrocyte membrane. These results were similar to those reported in another study [80], which showed good biocompatibility of the $MgFe_2O_4$ NPs.

The cytotoxicity of the $MgFe_2O_4$@ZOL NPs and MW treatment were assessed through a CCK-8 assay. The efficacy of the $MgFe_2O_4$@ZOL NPs showed concentration-dependent changes (Fig. 5B). With increasing nanoparticle concentration, the viability of the A549 cells decreased, and after one day of treatment with 100 μg/mL $MgFe_2O_4$@ZOL NPs, the cell survival rate decreased to 70 %. There were prominent differences in the viability of cancer cells at different MW power levels. After A549 cells were cocultured with $MgFe_2O_4$ NPs for the uptake of nanoparticles, they were irradiated at different power levels (i.e., 0, 4, and 5 W) for 5 min to determine the optimum power of the MW to resist cancer cells. There was almost no difference between the A549 cells treated with MW at 4 W and the cells not treated with MW (Fig. 5C). However, after treatment with MW at 5 W, the cell viability decreased to 60 %; specifically, after treatment with 100 μg/mL $MgFe_2O_4$ NPs, the viability decreased to 30 %. These results can serve as a reference for the subsequent selection of the nanoparticle concentration and microwave power.

The proliferation of the cancer cells treated with the nanoparticles and irradiated with MW was evaluated through a live-dead staining assay. As displayed in Fig. 5D, no red fluorescence in the control group indicated no dead cells. The intensity of the red fluorescence of the cells treated with 100 μg/mL $MgFe_2O_4$ NPs was slightly stronger than that of the cells in the control group. Although green fluorescence dominated, the intensity of red fluorescence was greater after intervention with $MgFe_2O_4$@ZOL NPs or MW, because of the antitumor effect of ZOL released from $MgFe_2O_4$@ZOL and the consequence of MDT/MTT. The intensity of red fluorescence was considerably greater when cancer cells were treated with both MW and $MgFe_2O_4$ NPs. Almost no live cells were detected after treatment with MW combine with $MgFe_2O_4$@ZOL NPs due to the effects of the synergistic treatment of ZOL, MDT, and MTT. ImageJ was utilized to statistically analyze the viability of the cells after staining, enabling quantitative observation of the killing effect of $MgFe_2O_4$@ZOL NPs and MW on cancer cells (Figure S4H, with the numbers representing survival rates). These phenomena reflected the strong anticancer effects of the combination treatment.

### 3.7. Cell structure alteration

Based on the strong Fenton reaction and the microwave responsiveness of the $MgFe_2O_4$@ZOL NPs, we further investigated lung cancer cells via TEM to evaluate the degree of intracellular damage. A549 cells were analyzed via TEM after they were incubated with the nanoparticles for 24 h and with MW at 5 W for 5 min. In the absence of treatment, the cells exhibited normal-shaped cytomembrane, nucleus (red arrows), endoplasmic reticulum (blue arrows), and mitochondria (black arrows) without typical apoptotic features (Figs. 6A–1). In this study, 100 μg/mL nanoparticles were used to treat A549 cells. Dark granules (green arrows) were distributed in the cytoplasm after treatment with nanoparticles (Figs. 6A–2), which indicated that they were endocytosed. The diameter of the granules was approximately 340 nm, which matched the results of the DLS analysis. After endocytosis of the $MgFe_2O_4$ NPs, some mitochondria in the cells appeared slightly swollen (black arrows), indicating that the nanoparticles generated a small amount of ROS,

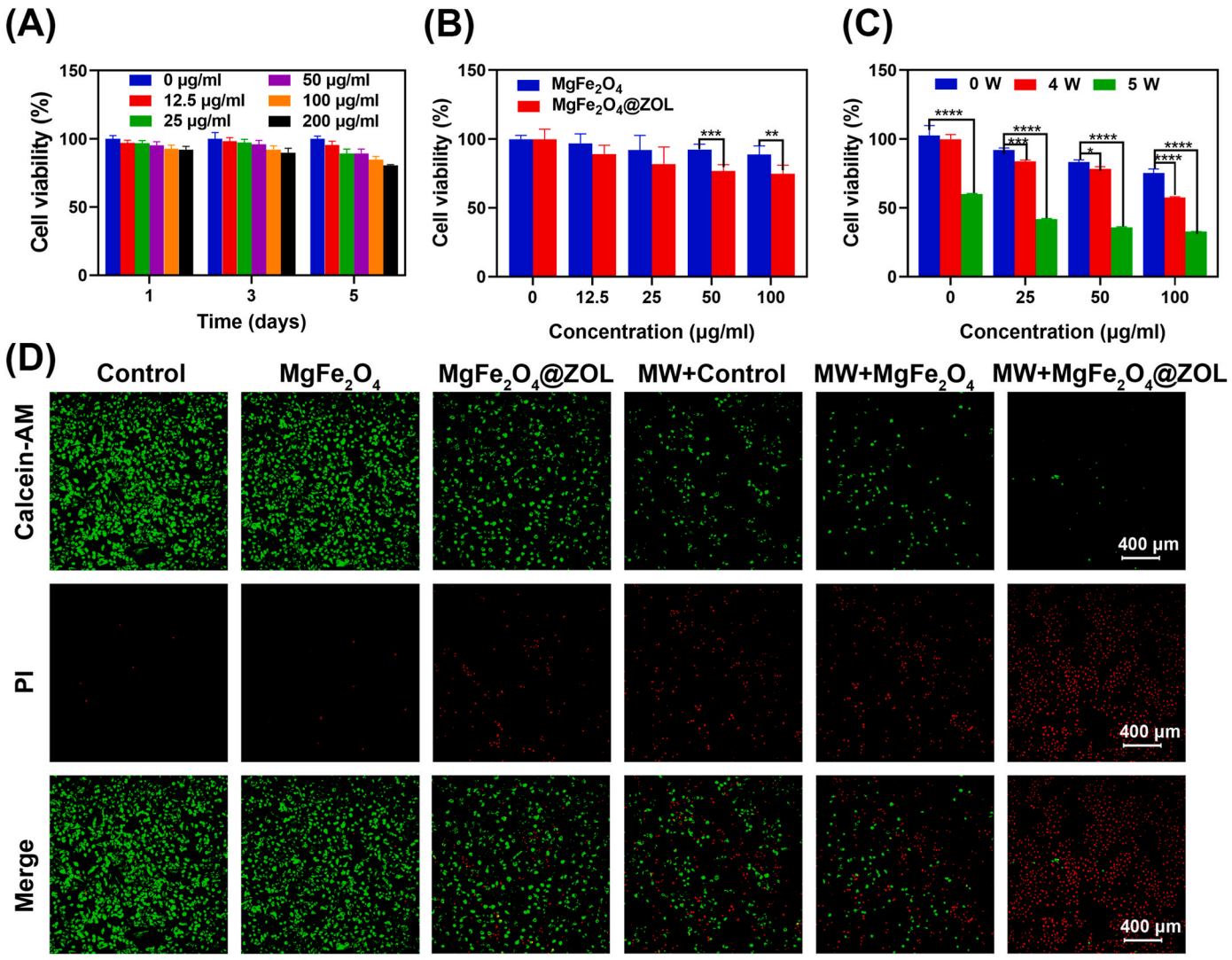


**Fig. 5.** The proliferation and viability of the tumor cells. (A) The cell proliferation of A549 cells treated with $MgFe_2O_4$ NPs for 1, 3, and 5 days. (B) The effects of $MgFe_2O_4$ NPs and $MgFe_2O_4$@ZOL NPs on A549 cell proliferation for 24 h. (C) Effects of $MgFe_2O_4$ NPs combined with MW irradiation on A549 cell proliferation. (D) The live/dead A549 cells staining with Calcein-AM/PI.

leading to impaired mitochondrial function. In the $MgFe_2O_4$@ZOL NP group, the mitochondria of the cells were more swollen, autophagosomes (yellow arrows), and lipid droplets (purple arrows) increased, and the chromatin appeared to be slightly condensed compared with $MgFe_2O_4$ NP group (Figs. 6A–3). After 5 min of 5 W MW irradiation, the A549 cells changed from normal fusiform to irregular round and even lysed. As shown in Figs. 6A–4 and 5, the lung cancer cell lost its normal morphology and exhibited more severe mitochondrial swelling, ridges detachment, vacuolization; expansion of the endoplasmic reticulum, degranulation; chromatin clumping, and edge aggregation; and the appearance of the lipid droplets, apoptotic body, and autophagosomes. The above manifestations occur due to the effects of ROS, ZOL, and hyperthermia, which disrupt oxidative phosphorylation and mitochondrial membrane permeability, leading to cellular damage, degeneration, and apoptosis [81]. As depicted in Fig. 6A–6, the high toxicity of the combination therapy leads to the direct disintegration and necrosis of tumor cells. Li et al. reported that magnetic $Fe_3O_4$ NPs could activate the IRE1-ASK1-JNK pathway and induce endoplasmic reticulum stress to triggers intrinsic apoptosis to enhance MWA [82]. TEM revealed membrane blebbing and apoptotic bodies, similar to the findings described by Li. The magnetic $MgFe_2O_4$ NPs and $Fe_3O_4$ NPs are similar in structure and characteristics. In addition, ZOL can lead to apoptosis through increased oxidative stress and endoplasmic reticulum stress [83]. Consequently, the combination of $MgFe_2O_4$@ZOL and MW not only enhances the cytotoxic effect of MTT on tumor tissues, but also induces mitochondrial damage and endoplasmic reticulum stress through the production of abundant ROS, hyperthermia, and ZOL, promoting programmed cell death in cancer cells and thus further enhancing antitumor efficacy.

### 3.8. *Anticancer effects in vitro*

For programmed cell death, cancer cell apoptosis is a crucial process that can be triggered by ROS and hyperthermia (Fig. 6B). For a more comprehensive understanding of the health and status of cells treated with the $MgFe_2O_4$@ZOL NPs, cell viability and apoptosis were detected using flow cytometry. The Annexin V-FITC and PI kits were utilized to assess the integrity of the cell membranes, and the analysis was conducted by fluorescence-activated cell sorting (Fig. 6C and D). The trend described above was reflected in the cancer cell apoptosis rate after the different treatments. The percentage of apoptotic cells significantly increased after MW irradiation. Specifically, in the MW control group, the percentage of apoptotic cells increased from 7.65 % to 41.24 %. In the MW + $MgFe_2O_4$ NP group, the percentage of apoptotic cells

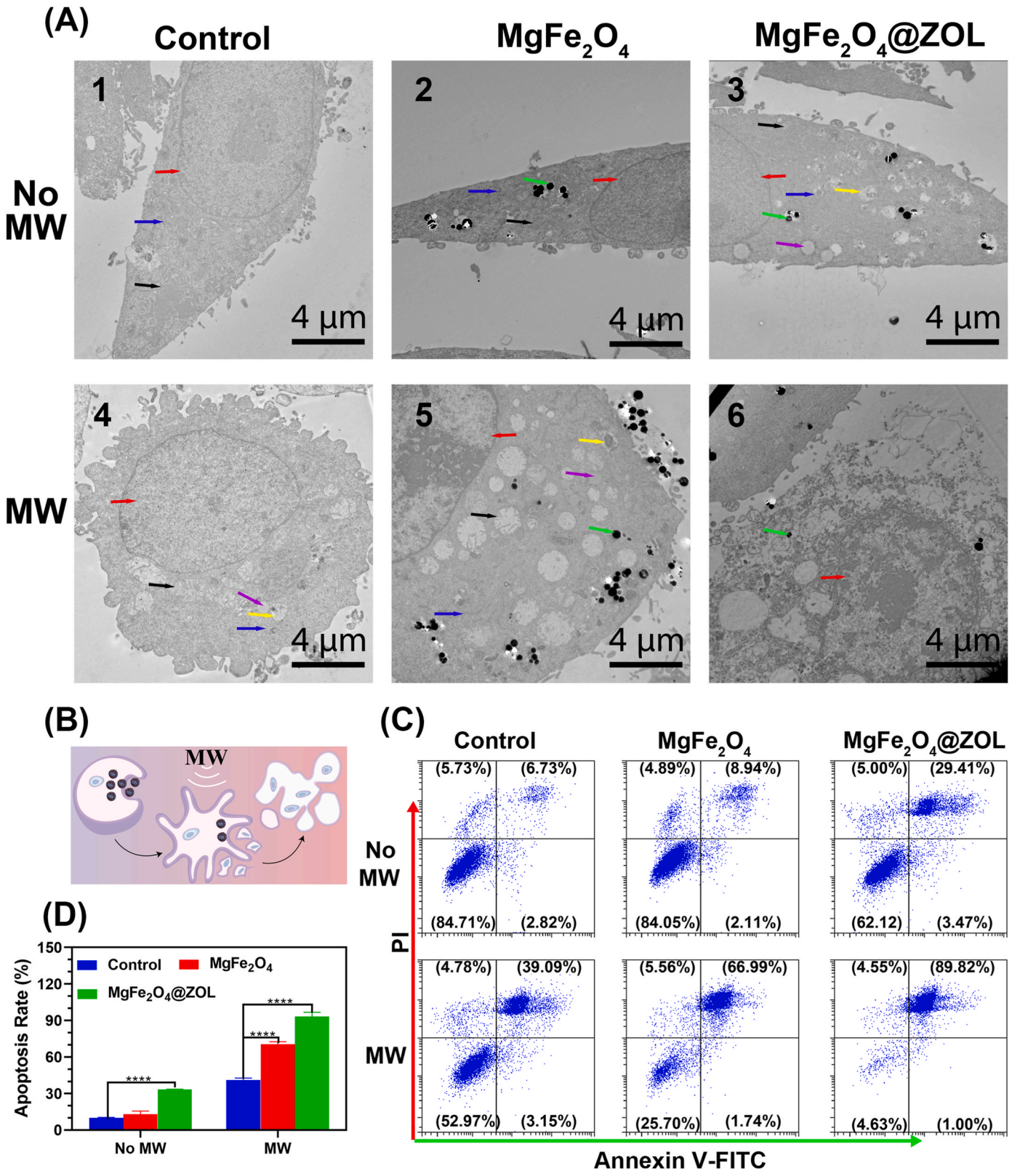


**Fig. 6.** In vitro anticancer effects. (A) TEM was used to detect the treatment of A549 cells: (A-1) Blank control; (A-2) $MgFe_2O_4$ NPs; (A-3) $MgFe_2O_4$@ZOL NPs; (A-4) MW control; (A-5) MW + $MgFe_2O_4$, and (A-6) MW + $MgFe_2O_4$@ZOL. (Red arrow indicates the cell nucleus, blue arrow indicates the endoplasmic reticulum, black arrow indicates the mitochondria, green arrow indicates the nanoparticles, and purple arrow indicates the lipid droplets.) (B) The diagram of cancer cell apoptosis process. (C) Fow cytometry was conducted to show the apoptosis of A549 cells in different treatment groups. (D) The apoptosis rate in different groups.

increased from 11.05 % to 68.73 %. The percentage of apoptotic cells in the MW + $MgFe_2O_4$@ZOL NP group increased from 32.87 % to 90.82 %. These findings indicated that synergistic therapy with $MgFe_2O_4$@ZOL NPs and MW effectively induced cell apoptosis through the combined effects of ZOL, ROS, and hyperpyrexia.

Since cancer metastasis and poor clinical prognosis are associated with proliferation and invasion of cancer cells, we analyzed the effects of $MgFe_2O_4$@ZOL and MW on the behavior of cancer cells, including proliferation, migration, and invasion of cells. The capacity for cancer cell proliferation was reflected in colony formation (Fig. 7A and D), and the colony formation rate of the cells in the MW + $MgFe_2O_4$@ZOL group decreased to 9 %. The invasion capability of the A549 cells was assessed through a transwell assay (Fig. 7B and E). The invasion assay revealed that the number of invasive cells in the control group was approximately 43, whereas, in the MW + $MgFe_2O_4$@ZOL group, it was approximately 7. Additionally, the migration area of the cells in the control, $MgFe_2O_4$, and $MgFe_2O_4$@ZOL groups was evaluated at 12 h and 24 h (Fig. 7C and F). At 12 h, the migration area of the cells in the control group was approximately 27 %, whereas that of the cells in the $MgFe_2O_4$@ZOL group was approximately 9 %. After 24 h, the migration area of the cells in the control group increased to approximately 60 %, while that of the cells in the $MgFe_2O_4$@ZOL group increased to 19 %.

It is well known that the uncontrolled energy of cancer cells for mitochondrial dysfunction induces cancer progression and invasion [84]. Our results demonstrated that the combination of $MgFe_2O_4$@ZOL NPs and MW inhibited the proliferation, migration and invasion of lung cancer cells. These effects may be attributed to the ability of ROS and hyperthermia to disrupt electron transport chains and destroy oxidative phosphorylation, leading to cell apoptosis. Furthermore, hyperthermia can interfere with the transcription of cancer cell DNA, thereby inhibiting the ability of cancer cells to proliferate and invade other tissues or organs, further enhancing antitumor effects [85,86].

### 3.9. Osteogenic differentiation

Osteogenic differentiation is an important process in the bone microenvironment. The evaluation was performed after the induction of osteogenic differentiation on days 3, 7, and 14. Alkaline phosphatase (ALP) staining was used to observe osteoblast differentiation and function, to assess the osteogenic differentiation of cells. Although there was no significant difference between the groups on day 3, the differences in ALP activity among the three groups increased substantially as the induction period increased (Fig. 8A–C). Alizarin red staining was utilized to identify mineralized nodule formation, providing a visual assessment of osteogenic induction effectiveness. The formation of mineralized nodules in the $MgFe_2O_4$ group increased remarkably in the C3H10 cells, whereas the mineralization in the $MgFe_2O_4$@ZOL group exhibited an even greater increase, with the effect becoming more pronounced over time (Fig. 8D–F). These changes occurred due to the synergistic stimulation of osteogenesis by the combined effects of $Mg^{2+}$ and ZOL [87,88]. Osteolytic bone destruction is common in lung or breast cancer patients with bone metastasis, because cancer cells secrete humoral factors that stimulate osteoclasts and inhibit osteoblasts to cause osteolytic bone destruction and induce SREs [4]. $Mg^{2+}$ mainly promotes the differentiation and adhesion of osteoblasts and enhances the adhesion of human bone-derived cells. Recently, Zhao et al. reported that a hydrogel microsphere (GelMA-BP-Mg) stimulates osteoblasts and endothelial cells while restraining osteoclasts via magnet-inspired $Mg^{2+}$ for the treatment of osteoporotic bone defects [89]. $MgFe_2O_4$@ZOL released $Mg^{2+}$ and ZOL in bone tumor tissues under MW irradiation to promote osteogenesis and inhibit osteoclasts. Thus, the inhibitory effects of $MgFe_2O_4$@ZOL NPs on osteoclasts should be further investigated. In other words, $MgFe_2O_4$@ZOL NPs were suitable for the treatment of osteolytic bone metastasis (such as lung cancer and breast cancer) to restore bone mineral density.

### 3.10. Efficacy of anticancer effects in vivo

Based on the excellent therapeutic efficacy and MW sensitivity in vitro, the performance of the combinations of targeting, MTT, CDT, and MDT enhanced by the $MgFe_2O_4$@ZOL NPs in vivo against tumors in nude mice was further evaluated. The nude mice bearing tumors were randomly assigned to the following groups: 1. PBS; 2. $MgFe_2O_4$ NPs; 3. $MgFe_2O_4$@ZOL NPs; 4. PBS + MW; 5. $MgFe_2O_4$ NPs + MW; 6. $MgFe_2O_4$@ZOL NPs + MW. The mice were administered solutions intravenously at a dosage of 2 mg/kg through the tail vein. Thermal

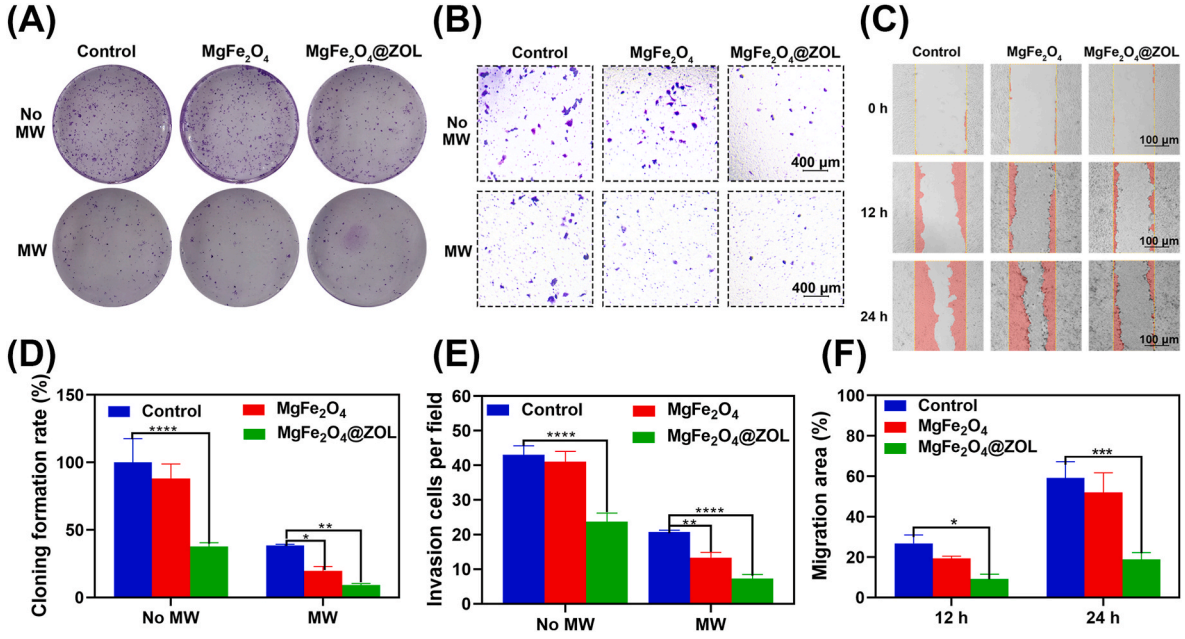


**Fig. 7.** Biological interactions between $MgFe_2O_4$@ZOL NPs and A549 cells in vitro. The A549 cells were treated with blank control, $MgFe_2O_4$, $MgFe_2O_4$@ZOL, MW + control, MW + $MgFe_2O_4$, and MW + $MgFe_2O_4$@ZOL. (A and D) Colony formation and clone formation rate. (B and E) Images of the transwell assay and invasion ability of A549. (C and F) Cell scratch assay and migration capability.

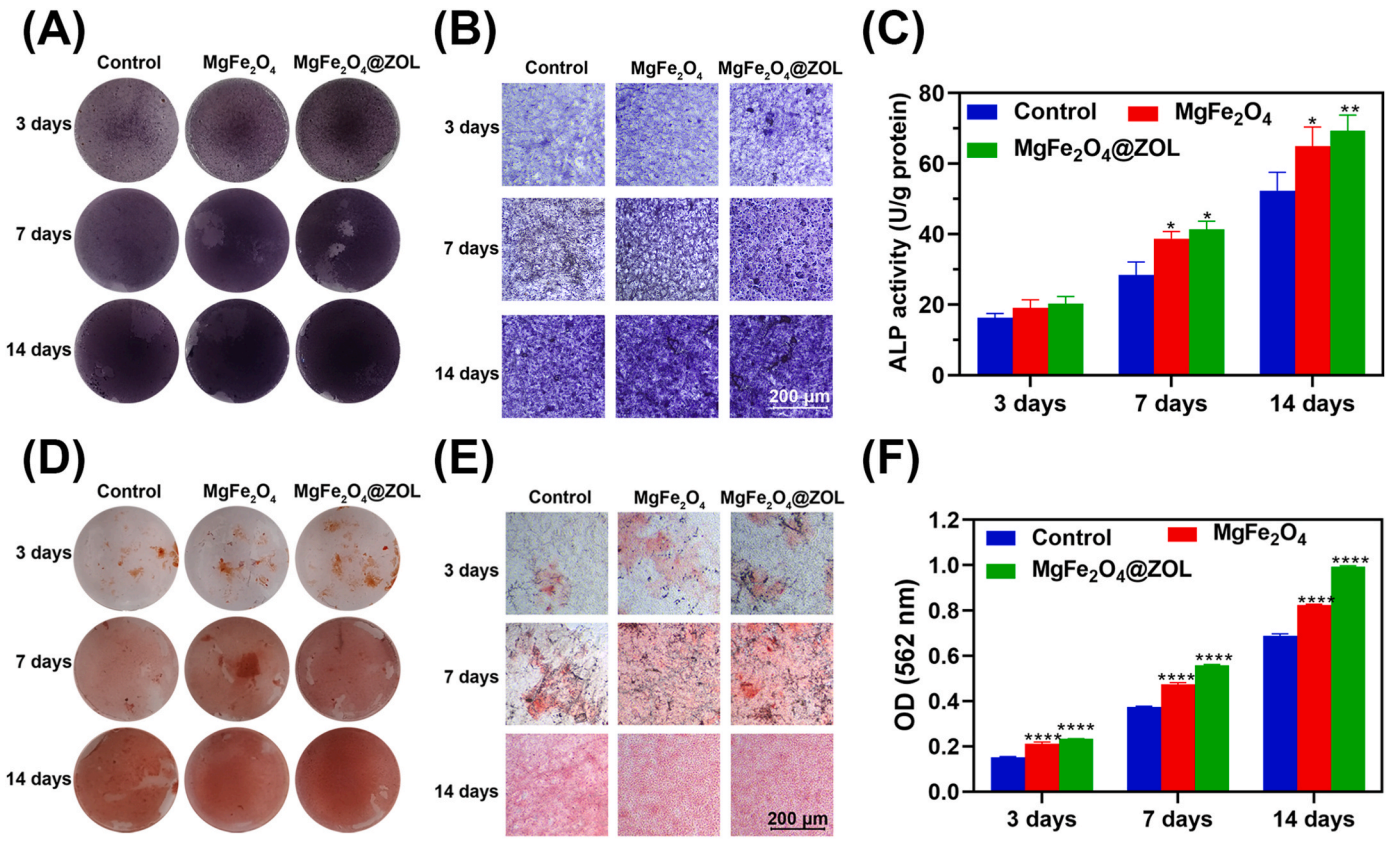


**Fig. 8.** Effects of $MgFe_2O_4$ and $MgFe_2O_4$@ZOL on the differentiation of osteoblasts in vitro. (A, B, and C) ALP activity of C3H10 cells on days 3, 7, and 14: (A) Macroscopic images; (B) Microscopic images; (C) Quantitative analysis of ALP activity. (D, E, and F) Alizarin red staining of C3H10 cells on days 3, 7, and 14: (D) Macroscopic images; (E) Microscopic images; (F) Quantitative analysis of mineralized nodules.

infrared images (Fig. 9A) and temperature changes were analyzed in the MW groups, and the ablation area of each group was quantitatively analyzed by imageJ software (Figure S4I). The heating area and temperature of the $MgFe_2O_4$ and $MgFe_2O_4$@ZOL groups were noticeably greater than those of the PBS group, and the area of $MgFe_2O_4$@ZOL group was larger than that of $MgFe_2O_4$ group. The in vivo temperature elevation curve is shown in Fig. 9D, with the $MgFe_2O_4$@ZOL group displaying the highest peak. These were partly attributed to the tumor-targeting ability, which facilitated the accumulation of the microwave sensitizer in tumors and enhanced the effect of selective MW heating [90,91]. In addition, the in vivo temperatures of all the groups were lower than the in vitro temperatures, probably because of greater heat dissipation caused by blood circulation [92]. These results indicated that the heating efficiency of tumors in the $MgFe_2O_4$@ZOL group was significantly increased after MW irradiation. The differences in body weight among the groups of mice were not statistically significant (Fig. 9E), which indicated that all the mice were in good condition. Fig. 9F showed that in the groups treated with $MgFe_2O_4$ NPs, the increase in tumor volume was slightly inhibited compared to that in the PBS group, and the tumors were found to grow rapidly. The group that was treated with $MgFe_2O_4$@ZOL NPs and MW exhibited significant tumor growth inhibition, probably due to the synergistic effects of the combination of ZOL, MDT, and MTT. The macroscopic images of the tumor and the tumor mass (Fig. 9B and C) in each group on day 14 confirmed these findings. The tumor sections were histologically stained to validate the effectiveness of various treatments in vivo (Fig. 9G–J). Prussian blue staining (Fig. 9G) was performed on tumor slices to evaluate the distribution of $Fe^{3+}$ released by $MgFe_2O_4$ NPs in the animals. These results demonstrated that there was a higher concentration of $Fe^{3+}$ in the tumor sites of the $MgFe_2O_4$@ZOL NPs group, suggesting that they possess a certain degree of tumor targeting capability. The histological images of tissues stained with hematoxylin and eosin (H&E) revealed remarkable necrosis in the tumor tissue in the $MgFe_2O_4$@ZOL + MW group, in stark contrast to the other groups (Fig. 9H). Furthermore, TUNEL staining of cells in the $MgFe_2O_4$@ZOL + MW group also exhibited a pronounced red fluorescence which represents apoptotic cells, suggestive of the multimodal combination therapy's superior ability to effectively induce cancer cell apoptosis compared to other treatment modalities (Fig. 9I). Additionally, Ki67 staining was carried out to assess the proliferation ability of cancer cells. The finding from Ki67 staining revealed a significant suppression in the synthesis of the nuclear proliferation protein Ki67 within the tumors of the $MgFe_2O_4$@ZOL + MW group, indicating that the multi-synergistic treatment exhibited promising anticancer efficacy in vivo (Fig. 9J). Histological staining of the major organs was conducted to determine whether adverse effects on the mice occurred throughout the treatment period (Figure S5). The findings revealed that there were no notable pathological alterations detected in the vital organs across all groups, indicating the absence of apparent side effects in the mice throughout the entire course of treatment.

## 4. Conclusion

To summarize, a novel antitumor nanoplatform, $MgFe_2O_4$@ZOL, was synthesized based on targeting-tumor and microwave-sensitive nanoparticles to effectively treat lung cancer bone metastasis via CDT, MDT, and selective-MTT. The advanced $MgFe_2O_4$@ZOL nanosystems could release $Fe^{3+}$, $Mg^{2+}$, and ZOL in the TME and under microwave irradiation. These compounds not only catalyze the decomposition of $H_2O_2$ to generate abundant cytotoxic ROS and deplete GSH in tumor tissues, inducing cancer cell apoptosis, but also stimulate osteogenesis to improve osteolytic destruction. In addition, the combination of

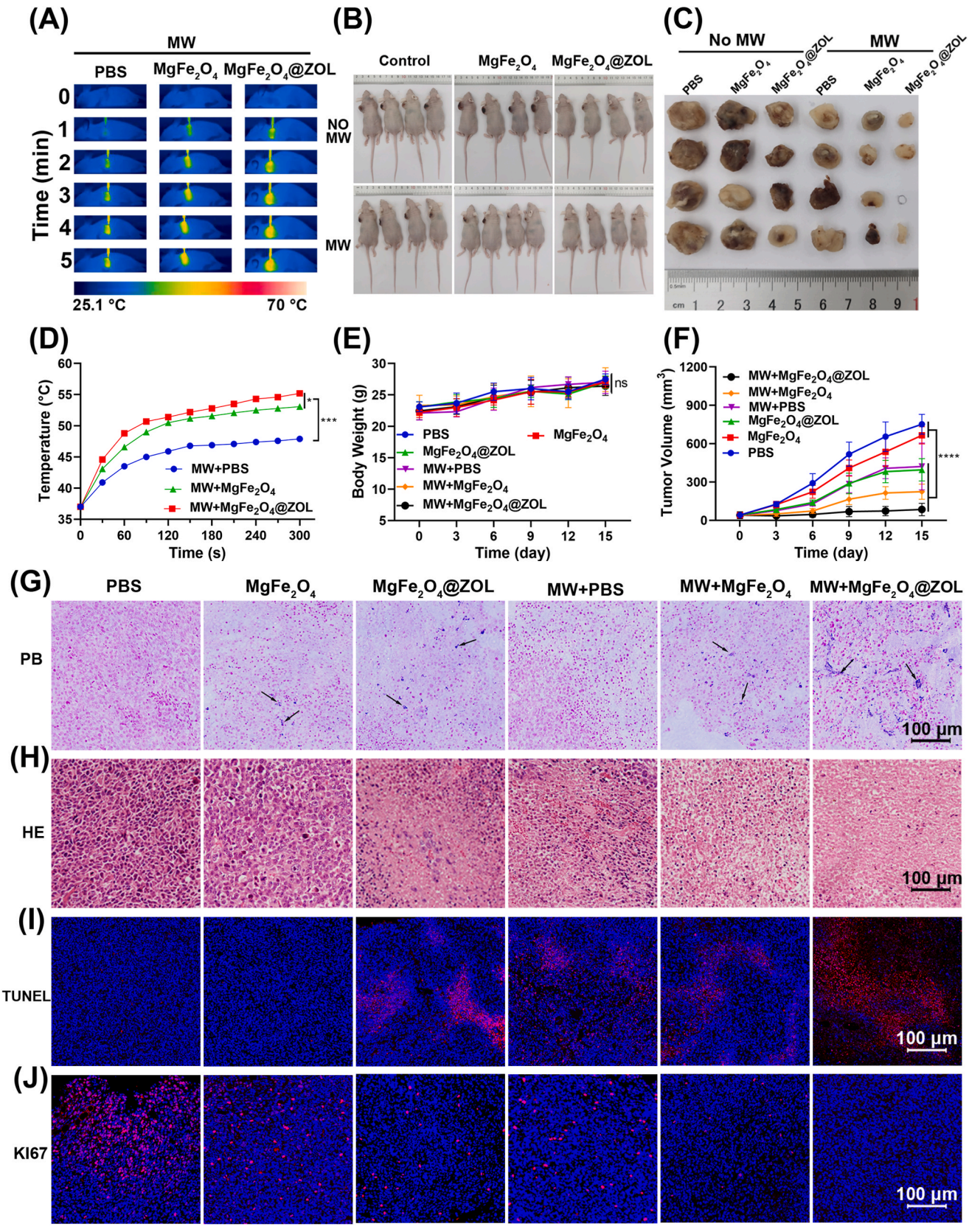


**Fig. 9.** In vivo antitumor effects. (A) Images of microwave heating in vivo. (B) Nude mice with tumor at the end of the experiment. (C) Images of tumors excised from mice. (D) Temperature changes caused by microwave heating in vivo. (E) Weight gain in various groups of mice. (F) The increase in tumor volume in mice between groups. (F) The tumor slices were stained with Prussian blue. (G) The tumor slices were stained with Prussian blue (PB) (the arrow points to the dyed $Fe^{3+}$). (H–J) H&E, TUNEL, and KI67 staining of tumor tissue between groups: (H) H&E staining; (I) TUNEL staining; (J) Ki67 staining.

$MgFe_2O_4$@ZOL and MWA further enhanced the release of ROS and selectively heated the tumor tissue to avoid damage to the surrounding tissues. Thus, this novel strategy is a promising candidate for treating lung cancer bone metastasis.

## Data availability statement

The data that support the findings of this study are available from the corresponding author upon reasonable request.

## Ethics approval

The Animal Ethics Committee of the General Hospital of Southern Theatre Command authorized all animal experimental procedures (ethical code SYDW2023007).

## CRediT authorship contribution statement

**Man Shu:** Writing – original draft, Validation, Software, Methodology, Data curation, Conceptualization. **Jingguang Wang:** Software, Methodology. **Ziyang Xu:** Visualization, Methodology. **Teliang Lu:** Methodology, Software. **Yue He:** Software, Methodology. **Renshan Li:** Methodology. **Guoqing Zhong:** Supervision, Methodology. **Yunbo Yan:** Visualization, Software. **Yu Zhang:** Supervision, Resources, Project administration. **Xiao Chu:** Writing – review & editing, Supervision, Resources, Conceptualization. **Jin Ke:** Resources, Project administration, Funding acquisition, Conceptualization.

## Declaration of competing interest

The authors declare no conflict of interest.

## Acknowledgements

We are grateful for the support from National Natural Science Foundation of China (U21A2084) and National Key Research and Development Program of China (2021YFC2400704).

## Appendix ASupplementary data

Supplementary data to this article can be found online at https://doi.org/10.1016/j.bioactmat.2024.04.016.

## References

[1] R.L. Siegel, K.D. Miller, N.S. Wagle, A. Jemal, Cancer statistics, 2023, CA A Cancer J. Clin. 73 (2023) 17–48.
[2] H. Brody, Lung cancer, Nature 587 (2020) S7.
[3] R.E. Coleman, Metastatic bone disease: clinical features, pathophysiology and treatment strategies, Cancer Treat Rev. 27 (2001) 165–176.
[4] G.R. Mundy, Mechanisms of osteolytic bone destruction, Bone 12 (Suppl 1) (1991) S1–S6.
[5] I.M. Adjei, M.N. Temples, S.B. Brown, B. Sharma, Targeted nanomedicine to treat bone metastasis, Pharmaceutics 10 (2018) 205.
[6] J. Fornetti, A.L. Welm, S.A. Stewart, Understanding the bone in cancer metastasis, J. Bone Miner. Res. 33 (2018) 2099–2113.
[7] Y. He, W. Luo, Y. Liu, Y. Wang, C. Ma, Q. Wu, P. Tian, D. He, Z. Jia, X. Lv, Y.S. Ma, H. Yang, K. Xu, X. Zhang, Y. Xiao, P. Zhang, Y. Liang, D. Fu, F. Yao, G. Hu, IL-20RB mediates tumoral response to osteoclastic niches and promotes bone metastasis of lung cancer, J. Clin. Invest. 132 (2022) e157917.
[8] M.A. Lopez-Olivo, N.A. Shah, G. Pratt, J.M. Risser, E. Symanski, M.E. Suarez-Almazor, Bisphosphonates in the treatment of patients with lung cancer and metastatic bone disease: a systematic review and meta-analysis, Support. Care Cancer 20 (2012) 2985–2998.
[9] W. Sun, K. Ge, Y. Jin, Y. Han, H. Zhang, G. Zhou, X. Yang, D. Liu, H. Liu, X.J. Liang, J. Zhang, Bone-targeted nanoplatform combining zoledronate and photothermal therapy to treat breast cancer bone metastasis, ACS Nano 13 (2019) 7556–7567.
[10] T. Ge, Z. Weiwei, F. Ge, L. Zhu, P. Song, W. Li, L. Gui, W. Dong, Y. Tao, K. Yang, A bone-targeting drug delivery vehicle of a metal–organic framework conjugate with zoledronate combined with photothermal therapy for tumor inhibition in cancer bone metastasis, Biomater. Sci. 10 (2022) 1831–1843.
[11] S.M. Jung, S. Han, H.Y. Kwon, Dose-intensity of bisphosphonates and the risk of osteonecrosis of the jaw in osteoporosis patients, Front. Pharmacol. 9 (2018) 796.
[12] E. Hatami, P.K. Bhusetty Nagesh, P. Chowdhury, S. Elliot, D. Shields, S. Chand Chauhan, M. Jaggi, M.M. Yallapu, Development of zoledronic acid-based nanoassemblies for bone-targeted anticancer therapy, ACS Biomater. Sci. Eng. 5 (2019) 2343–2354.
[13] B.D. Cardoso, A.R.O. Rodrigues, M. Banobre-Lopez, B.G. Almeida, C.O. Amorim, V. S. Amaral, P.J.G. Coutinho, E.M.S. Castanheira, Magnetoliposomes based on shape anisotropic calcium/magnesium ferrite nanoparticles as nanocarriers for doxorubicin, Pharmaceutics 13 (2021) 1248.
[14] D. Jiao, Y. Yao, Z. Li, J. Ren, X. Han, Simultaneous C-arm computed tomography-guided microwave ablation and cementoplasty in patients with painful osteolytic bone metastases: a single-center experience, Acad. Radiol. 29 (2022) 42–50.
[15] M. Shu, J. Ke, The surgical management of osteoid osteoma: a systematic review, Front. Oncol. 12 (2022) 935640.
[16] O. Seror, Ablative therapies: advantages and disadvantages of radiofrequency, cryotherapy, microwave and electroporation methods, or how to choose the right method for an individual patient? Diagnostic and interventional imaging 96 (2015) 617–624.
[17] G. Carrafiello, D. Laganà, M. Mangini, F. Fontana, G. Dionigi, L. Boni, F. Rovera, S. Cuffari, C. Fugazzola, Microwave tumors ablation: principles, clinical applications and review of preliminary experiences, Int. J. Surg. 6 (Suppl 1) (2008) S65–S69.
[18] R.L. Cazzato, G. de Rubeis, P. de Marini, D. Dalili, G. Koch, P. Auloge, J. Garnon, A. Gangi, Percutaneous microwave ablation of bone tumors: a systematic review, Eur. Radiol. 31 (2021) 3530–3541.
[19] Y. Zhu, Q. Li, C. Wang, Y. Hao, N. Yang, M. Chen, J. Ji, L. Feng, Z. Liu, Rational design of biomaterials to potentiate cancer thermal therapy, Chem. Rev. 123 (2023) 7326–7378.
[20] Q. Du, T. Ma, C. Fu, T. Liu, Z. Huang, J. Ren, H. Shao, K. Xu, F. Tang, X. Meng, Encapsulating ionic liquid and $Fe_3O_4$ nanoparticles in gelatin microcapsules as microwave susceptible agent for MR imaging-guided tumor thermotherapy, ACS Appl. Mater. Interfaces 7 (2015) 13612–13619.
[21] Z. Yang, L. Wang, Y. Liu, S. Liu, D. Tang, L. Meng, B. Cui, ZnO capped flower-like porous carbon-$Fe_3O_4$ composite as carrier for bi-triggered drug delivery, Mater. Sci. Eng., C 107 (2020) 110256.
[22] S. Tang, C. Fu, L. Tan, T. Liu, J. Mao, X. Ren, H. Su, D. Long, Q. Chai, Z. Huang, X. Chen, J. Wang, J. Ren, X. Meng, Imaging-guided synergetic therapy of orthotopic transplantation tumor by superselectively arterial administration of microwave-induced microcapsules, Biomaterials 133 (2017) 144–153.
[23] S.J. Salih, W.M. Mahmood, Review on magnetic spinel ferrite ($MFe_2O_4$) nanoparticles: from synthesis to application, Heliyon 9 (2023) e16601.
[24] H. Li, J. Sun, H. Zhu, H. Wu, H. Zhang, Z. Gu, K. Luo, Recent advances in development of dendritic polymer-based nanomedicines for cancer diagnosis, Wiley Interdiscip Rev Nanomed Nanobiotechnol 13 (2021) e1670.
[25] Y. Feng, Q. Chen, C. Jin, Y. Ruan, Q. Chen, W. Lin, C. Zhu, T. Zhang, Y. Zhang, J. Gao, J. Mo, Microwave-activated Cu-doped zirconium metal-organic framework for a highly effective combination of microwave dynamic and thermal therapy, J. Contr. Release 361 (2023) 102–114.
[26] H. Peng, M. Wang, C. Hu, J. Guo, A new type of $MgFe_2O_4$@CuS-APTES nanocarrier for magnetic targeting and light-microwave dual controlled drug release, Int. J. Nanomed. 15 (2020) 8783–8802.
[27] X. Li, Z. Duan, X. Chen, D. Pan, Q. Luo, L. Gu, G. Xu, Y. Li, H. Zhang, Q. Gong, R. Chen, Z. Gu, K. Luo, Impairing tumor metabolic plasticity via a stable metal-phenolic-based polymeric nanomedicine to suppress colorectal cancer, Adv. Mater. 35 (2023) e2300548.
[28] D. Ramnandan, S. Mokhosi, A. Daniels, M. Singh, Chitosan, polyethylene glycol and polyvinyl alcohol modified $MgFe_2O_4$ ferrite magnetic nanoparticles in doxorubicin delivery: a comparative study in vitro, Molecules 26 (2021) 3893.
[29] Y. Diao, Z. Yan, M. Guo, X. Wang, Magnetic multi-metal co-doped magnesium ferrite nanoparticles: an efficient visible light-assisted heterogeneous Fenton-like catalyst synthesized from saprolite laterite ore, J. Hazard Mater. 344 (2018) 829–838.
[30] M. Lopez-Lazaro, Dual role of hydrogen peroxide in cancer: possible relevance to cancer chemoprevention and therapy, Cancer Lett. 252 (2007) 1–8.
[31] E. Boedtkjer, S.F. Pedersen, The acidic tumor microenvironment as a driver of cancer, Annu. Rev. Physiol. 82 (2020) 103–126.
[32] Z. Tang, Y. Liu, M. He, W. Bu, Chemodynamic therapy: tumour microenvironment-mediated fenton and fenton-like reactions, Angew. Chem., Int. Ed. Engl. 58 (2019) 946–956.
[33] Y. Wang, F. Gao, X. Li, G. Niu, Y. Yang, H. Li, Y. Jiang, Tumor microenvironment-responsive fenton nanocatalysts for intensified anticancer treatment, J. Nanobiotechnol. 20 (2022) 69.
[34] Z. Tang, H. Zhang, Y. Liu, D. Ni, H. Zhang, J. Zhang, Z. Yao, M. He, J. Shi, W. Bu, Antiferromagnetic pyrite as the tumor microenvironment-mediated nanoplatform for self-enhanced tumor imaging and therapy, Adv. Mater. 29 (2017) 1701683.
[35] H. Wu, F. Chen, D. Gu, C. You, B. Sun, A pH-activated autocatalytic nanoreactor for self-boosting Fenton-like chemodynamic therapy, Nanoscale 12 (2020) 17319–17331.
[36] H. Zhou, Z. Liu, Z. Zhang, N.K. Pandey, E. Amador, W. Nguyen, L. Chudal, L. Xiong, W. Chen, Y. Wen, Copper-cysteamine nanoparticle-mediated microwave dynamic therapy improves cancer treatment with induction of ferroptosis, Bioact. Mater. 24 (2023) 322–330.
[37] H. Li, Y. Feng, Q. Luo, Z. Li, X. Li, H. Gan, Z. Gu, Q. Gong, K. Luo, Stimuli-activatable nanomedicine meets cancer theranostics, Theranostics 13 (2023) 5386–5417.

[38] H. Lou, L. Chu, W. Zhou, J. Dou, X. Teng, W. Tan, B. Zhou, A diselenium-bridged covalent organic framework with pH/GSH/photo-triple-responsiveness for highly controlled drug release toward joint chemo/photothermal/chemodynamic cancer therapy, J. Mater. Chem. B 10 (2022) 7955–7966.

[39] C. Jia, Y. Guo, F.G. Wu, Chemodynamic therapy via fenton and fenton-like nanomaterials: strategies and recent advances, Small 18 (2022) e2103868.

[40] D. Long, T. Liu, L. Tan, H. Shi, P. Liang, S. Tang, Q. Wu, J. Yu, J. Dou, X. Meng, Multisynergistic platform for tumor therapy by mild microwave irradiation-activated chemotherapy and enhanced ablation, ACS Nano 10 (2016) 9516–9528.

[41] Q. Wu, N. Xia, D. Long, L. Tan, W. Rao, J. Yu, C. Fu, X. Ren, H. Li, L. Gou, P. Liang, J. Ren, L. Li, X. Meng, Dual-functional supernanoparticles with microwave dynamic therapy and microwave thermal therapy, Nano Lett. 19 (2019) 5277–5286.

[42] A. Manohar, C. Krishnamoorthi, Photocatalytic study and superparamagnetic nature of Zn-doped $MgFe_2O_4$ colloidal size nanocrystals prepared by solvothermal reflux method, J. Photochem. Photobiol., B 173 (2017) 456–465.

[43] H. Gao, Z. Cao, H. Liu, L. Chen, Y. Bai, Q. Wu, X. Yu, W. Wei, M. Wang, Multifunctional nanomedicines-enabled chemodynamic-synergized multimodal tumor therapy via Fenton and Fenton-like reactions, Theranostics 13 (2023) 1974–2014.

[44] Y. Wang, X. Ren, Y. Zheng, L. Tan, B. Li, C. Fu, Q. Wu, Z. Chen, J. Ren, D. Yang, S. Yu, X. Meng, Boosting microwave thermo-dynamic cancer therapy of TiMOF via COF-coating, Small (2023) e2304440.

[45] Y. Huang, Z. Xiao, Z. Guan, Z. Zeng, Y. Shen, X. Xu, C. Zhao, Bone-seeking nanoplatform co-delivering cisplatin and zoledronate for synergistic therapy of breast cancer bone metastasis and bone resorption, Acta Pharm. Sin. B 10 (2020) 2384–2403.

[46] X. Gao, L. Li, X. Cai, Q. Huang, J. Xiao, Y. Cheng, Targeting nanoparticles for diagnosis and therapy of bone tumors: opportunities and challenges, Biomaterials 265 (2021) 120404.

[47] K.C. Valkenburg, M.R. Steensma, B.O. Williams, Z. Zhong, Skeletal metastasis: treatments, mouse models, and the Wnt signaling, Chin. J. Cancer 32 (2013) 380–396.

[48] E. Boanini, P. Torricelli, M. Gazzano, M. Fini, A. Bigi, The effect of zoledronate-hydroxyapatite nanocomposites on osteoclasts and osteoblast-like cells in vitro, Biomaterials 33 (2012) 722–730.

[49] K. Ramanlal Chaudhari, A. Kumar, V.K. Megraj Khandelwal, M. Ukawala, A. S. Manjappa, A.K. Mishra, J. Monkkonen, R.S. Ramachandra Murthy, Bone metastasis targeting: a novel approach to reach bone using Zoledronate anchored PLGA nanoparticle as carrier system loaded with Docetaxel, J. Contr. Release 158 (2012) 470–478.

[50] H. Qiao, Z. Cui, S. Yang, D. Ji, Y. Wang, Y. Yang, X. Han, Q. Fan, A. Qin, T. Wang, X.P. He, W. Bu, T. Tang, Targeting osteocytes to attenuate early breast cancer bone metastasis by theranostic upconversion nanoparticles with responsive plumbagin release, ACS Nano 11 (2017) 7259–7273.

[51] R. Coleman, R. Cook, V. Hirsh, P. Major, A. Lipton, Zoledronic acid use in cancer patients: more than just supportive care? Cancer 117 (2011) 11–23.

[52] W. Sun, Y. Han, Z. Li, K. Ge, J. Zhang, Bone-targeted mesoporous silica nanocarrier anchored by zoledronate for cancer bone metastasis, Langmuir 32 (2016) 9237–9244.

[53] Z. Li, H. Li, C. Shi, M. Yu, L. Wei, Z. Ni, Nanomolar colorimetric quantitative detection of $Fe^{3+}$ and PPi with high selectivity, Spectrochim. Acta Mol. Biomol. Spectrosc. 159 (2016) 249–253.

[54] X. Wang, Y. Cai, C. Wu, J. Liang, K. Tang, Z. Lin, L. Chen, Y. Lu, Q. Wang, Conversion of senescent cartilage into a pro-chondrogenic microenvironment with antibody-functionalized copper sulfate nanoparticles for efficient osteoarthritis therapy, J. Nanobiotechnol. 21 (2023) 258.

[55] D.H. de Hoyos-Sifuentes, P.J. Reséndiz-Hernández, J.A. Díaz-Guillén, R.M. Ochoa-Palacios, G. Altamirano-Guerrero, Synthesis and characterization of MgFe2O4 nanoparticles and PEG-coated MgFe2O4 nanocomposite, J. Mater. Res. Technol. 18 (2022) 3130–3142.

[56] F. Tang, L. Li, D. Chen, Mesoporous silica nanoparticles: synthesis, biocompatibility and drug delivery, Adv. Mater. 24 (2012) 1504–1534.

[57] Y. Jin, X. Liang, Y. An, Z. Dai, Microwave-triggered smart drug release from liposomes Co-encapsulating doxorubicin and salt for local combined hyperthermia and chemotherapy of cancer, Bioconjugate Chem. 27 (2016) 2931–2942.

[58] Y. Li, X. Dong, X. Yu, Magentic energy losses and temperature control system for giant magnetostrictive transducer, Micromachines 14 (2023) 177.

[59] V.M. Khot, A.B. Salunkhe, N.D. Thorat, R.S. Ningthoujam, S.H. Pawar, Induction heating studies of dextran coated $MgFe_2O_4$ nanoparticles for magnetic hyperthermia, Dalton Trans. 42 (2013) 1249–1258.

[60] Z. Wang, B. Liu, J. Tu, J. Xiang, H. Xiong, Y. Wu, S. Ding, D. Zhu, D. Zhu, F. Liu, G. Hu, X. Yuan, PLGA nanoparticles loaded with sorafenib combined with thermosensitive hydrogel system and microwave hyperthermia for multiple sensitized radiotherapy, Pharmaceutics 15 (2023) 487.

[61] R. Ravi, A. MishraAnamika, S. Ahmad, Fabrication of superparamagnetic bimetallic magnesium nanoferrite using green polyol: characterization and anticancer analysis in vitro on lung cancer cell line A549, ACS Appl. Bio Mater. 5 (2022) 5365–5376.

[62] X. Xu, Q. Wu, L. Tan, X. Men, Y. Huang, H. Li, Biomimetic metal-chalcogenide agents enable synergistic cancer therapy via microwave thermal-dynamic therapy and immune cell activation, ACS Appl. Mater. Interfaces 15 (2023) 42182–42195.

[63] L. John, M. Janeta, S. Szafert, Designing of macroporous magnetic bioscaffold based on functionalized methacrylate network covered by hydroxyapatites and doped with nano-$MgFe_2O_4$ for potential cancer hyperthermia therapy, Mater. Sci. Eng., C 78 (2017) 901–911.

[64] L. Liu, H. Jiang, J. Dong, W. Zhang, G. Dang, M. Yang, Y. Li, H. Chen, H. Ji, L. Dong, PEGylated $MoS_2$ quantum dots for traceable and pH-responsive chemotherapeutic drug delivery, Colloids Surf. B Biointerfaces 185 (2020) 110590.

[65] K. Ramanlal Chaudhari, A. Kumar, V.K. Megraj Khandelwal, M. Ukawala, A. S. Manjappa, A.K. Mishra, J. Monkkonen, R.S. Ramachandra Murthy, Bone metastasis targeting: a novel approach to reach bone using Zoledronate anchored PLGA nanoparticle as carrier system loaded with Docetaxel, J. Contr. Release 158 (2012) 470–478.

[66] X. Ma, X. Ren, X. Guo, C. Fu, Q. Wu, L. Tan, H. Li, W. Zhang, X. Chen, H. Zhong, X. Meng, Multifunctional iron-based Metal-Organic framework as biodegradable nanozyme for microwave enhancing dynamic therapy, Biomaterials 214 (2019) 119223.

[67] M. Kara, T. Boran, E. Oztas, A.T. Jannuzzi, S. Ozden, G. Ozhan, Zoledronic acid-induced oxidative damage and endoplasmic reticulum stress-mediated apoptosis in human embryonic kidney (HEK-293) cells, J. Biochem. Mol. Toxicol. 36 (2022) e23083.

[68] Y. Xiong, C. Xiao, Z. Li, X. Yang, Engineering nanomedicine for glutathione depletion-augmented cancer therapy, Chem. Soc. Rev. 50 (2021) 6013–6041.

[69] X. Cheng, H.D. Xu, H.H. Ran, G. Liang, F.G. Wu, Glutathione-depleting nanomedicines for synergistic cancer therapy, ACS Nano 15 (2021) 8039–8068.

[70] B. Niu, K. Liao, Y. Zhou, T. Wen, G. Quan, X. Pan, C. Wu, Application of glutathione depletion in cancer therapy: enhanced ROS-based therapy, ferroptosis, and chemotherapy, Biomaterials 277 (2021) 121110.

[71] Z. Lan, K. Chai, Y. Jiang, X. Liu, Characterization of urinary biomarkers and their relevant mechanisms of zoledronate-induced nephrotoxicity using rats and HK-2 cells, Hum. Exp. Toxicol. 38 (2019) 598–609.

[72] X. Qu, Z. Sun, Y. Wang, H.S. Ong, Zoledronic acid promotes osteoclasts ferroptosis by inhibiting FBXO9-mediated p53 ubiquitination and degradation, PeerJ 9 (2021) e12510.

[73] L. Kennedy, J.K. Sandhu, M.E. Harper, M. Cuperlovic-Culf, Role of glutathione in cancer: from mechanisms to therapies, Biomolecules 10 (2020) 1429.

[74] W. Al-Gethami, N. Al-Qasmi, S.H. Ismail, A.H. Sadek, QCM-based $MgFe_2O_4$@CaAlg nanocomposite as a fast response nanosensor for real-time detection of methylene blue dye, Nanomaterials 13 (2022) 97.

[75] X. Chu, L. Zhang, Y. Li, Y. He, Y. Zhang, C. Du, NIR responsive doxorubicin-loaded hollow copper ferrite @ polydopamine for synergistic chemodynamic/photothermal/chemo-therapy, Small 19 (2023) e2205414.

[76] C. Zhang, W. Bu, D. Ni, S. Zhang, Q. Li, Z. Yao, J. Zhang, H. Yao, Z. Wang, J. Shi, Synthesis of iron nanometallic glasses and their application in cancer therapy by a localized fenton reaction, Angew Chem. Int. Ed. Engl. 55 (2016) 2101–2106.

[77] W. Wang, Y. Jin, Z. Xu, X. Liu, S.Z. Bajwa, W.S. Khan, H. Yu, Stimuli-activatable nanomedicines for chemodynamic therapy of cancer, Wiley Interdiscip Rev Nanomed Nanobiotechnol 12 (2020) e1614.

[78] N. Thomas, D.D. Dionysiou, S.C. Pillai, Heterogeneous Fenton catalysts: a review of recent advances, J. Hazard Mater. 404 (2021) 124082.

[79] F. Liu, L. Lin, Y. Zhang, Y. Wang, S. Sheng, C. Xu, H. Tian, X. Chen, A tumor-microenvironment-activated nanozyme-mediated theranostic nanoreactor for imaging-guided combined tumor therapy, Adv. Mater. 31 (2019) e1902885.

[80] A. Manohar, V. Vijayakanth, M.R. Pallavolu, K.H. Kim, Effects of Ni - substitution on structural, magnetic hyperthermia, photocatalytic and cytotoxicity study of $MgFe_2O_4$ nanoparticles, J. Alloys Compd. 879 (2021) 160515.

[81] M.H. Cheng, H.L. Huang, Y.Y. Lin, K.H. Tsui, P.C. Chen, S.Y. Cheng, I.W. Chong, P. J. Sung, M.H. Tai, Z.H. Wen, N.F. Chen, H.M. Kuo, BA6 induces apoptosis via stimulation of reactive oxygen species and inhibition of oxidative phosphorylation in human lung cancer cells, Oxid. Med. Cell. Longev. 2019 (2019) 6342104.

[82] S. Li, Y. Liu, X. Liu, B. Lan, W. Li, F. Guo, Magnetite $Fe_3O_4$ nanoparticles enhance mild microwave ablation of tumor by activating the IRE1-ASK1-JNK pathway and inducing endoplasmic reticulum stress, Int. J. Nanomed. 16 (2021) 6129–6140.

[83] M. Kara, T. Boran, E. Oztas, A.T. Jannuzzi, S. Ozden, G. Ozhan, Zoledronic acid-induced oxidative damage and endoplasmic reticulum stress-mediated apoptosis in human embryonic kidney (HEK-293) cells, J. Biochem. Mol. Toxicol. 36 (2022) e23083.

[84] C.C. Hsu, L.M. Tseng, H.C. Lee, Role of mitochondrial dysfunction in cancer progression, Exp. Biol. Med. 241 (2016) 1281–1295.

[85] M.B. Ahmed, A.A.A. Alghamdi, S.U. Islam, H. Ahsan, Y.S. Lee, The complex roles of DNA repair pathways, inhibitors, hyperthermia, and contact inhibition in cell cycle halts, Mini Rev. Med. Chem. 23 (2023) 514–529.

[86] S. Cadenas, Mitochondrial uncoupling, ROS generation and cardioprotection, Biochim. Biophys. Acta Bioenerg. 1859 (2018) 940–950.

[87] X. Wei, W. Zhou, Z. Tang, H. Wu, Y. Liu, H. Dong, N. Wang, H. Huang, S. Bao, L. Shi, X. Li, Y. Zheng, Z. Guo, Magnesium surface-activated 3D printed porous PEEK scaffolds for in vivo osseointegration by promoting angiogenesis and osteogenesis, Bioact. Mater. 20 (2023) 16–28.

[88] Z. Ran, Y. Wang, J. Li, W. Xu, J. Tan, B. Cao, D. Luo, Y. Ding, J. Wu, L. Wang, K. Xie, L. Deng, P. Fu, X. Sun, L. Shi, Y. Hao, 3D-printed biodegradable magnesium alloy scaffolds with zoledronic acid-loaded ceramic composite coating promote osteoporotic bone defect repair, International Journal of Bioprinting 9 (2023) 769.

[89] Z. Zhao, G. Li, H. Ruan, K. Chen, Z. Cai, G. Lu, R. Li, L. Deng, M. Cai, W. Cui, Capturing magnesium ions via microfluidic hydrogel microspheres for promoting cancellous bone regeneration, ACS Nano 15 (2021) 13041–13054.

[90] S.B. Bai, Y. Cheng, D.Z. Liu, Q.F. Ji, M. Liu, B.L. Zhang, Q.B. Mei, S.Y. Zhou, Bone-targeted PAMAM nanoparticle to treat bone metastases of lung cancer, Nanomedicine 15 (2020) 833–849.
[91] S. Yukumi, Y. Watanabe, A. Horiuchi, T. Doi, K. Sato, M. Yoshida, Y. Yamamoto, T. Maehara, H. Aono, T. Naohara, K. Kawachi, Repeated inductive heating using a sintered MgFe2O4 needle for minimally invasive local control in breast cancer therapy, Int. J. Hyperther. 25 (2009) 416–421.
[92] N. Bhardwaj, A.D. Strickland, F. Ahmad, L. Atanesyan, K. West, D.M. Lloyd, A comparative histological evaluation of the ablations produced by microwave, cryotherapy and radiofrequency in the liver, Pathology 41 (2009) 168–172.